Zinc alloy-based bone internal fixation screw with antibacterial and anti-osteolytic properties

Xinhua Qu [a,b,1], Hongtao Yang [c,d,1], Bo Jia [b,f,1], Minqi Wang [a,b], Bing Yue [a], Yufeng Zheng [c,e,**], Kerong Dai [b,*]

[a] Department of Bone and Joint Surgery, Department of Orthopedics, Renji Hospital, School of Medicine, Shanghai Jiao Tong University, Shanghai 200127, China
[b] Department of Orthopedics, Shanghai Key Laboratory of Orthopedic Implant, Shanghai Ninth People's Hospital, Shanghai Jiao Tong University School of Medicine, Shanghai 200011, China
[c] School of Materials Science and Engineering, Peking University, Beijing 100871, China
[d] School of Engineering Medicine, Beihang University, Beijing 100191, China
[e] International Research Organization for Advanced Science and Technology, Kumamoto University, 2-39-1 Kurokami, Chuo-Ku, Kumamoto 860-8555, Japan
[f] Department of Orthopedics, Shanghai General Hospital, Shanghai Jiao Tong University School of Medicine, Shanghai 200080, China

ARTICLE INFO

ABSTRACT

There is no targeted effective treatment for patients undergoing internal fixation surgery/two-stage total joint revision surgery with a high risk of postoperative infection and osteolysis, while the rate of reoperation due to infection and osteolysis remains high. In this study, we report a pioneering application of implants made of biodegradable Zn–Ag alloy with active antibacterial and anti-osteolytic properties in three classical animal models, illustrating antibacterial, anti-osteolysis, and internal fixation for fractures. The antibacterial activity of the Zn–2Ag alloy was verified in a rat femur osteomyelitis prevention model, while the anti-osteolytic properties were evaluated using a mouse cranial osteolysis model. Moreover, the Zn–2Ag based screws showed similar performance in bone fracture fixation compared to the Ti–6Al–4V counterpart. The fracture healed completely after 3 months in the rabbit femoral condyle fracture model. Furthermore, the underlying antibacterial mechanism may include inhibition of biofilm formation, autolysis-related pathways, and antibiotic resistance pathways. Osseointegration mechanisms may include inhibition of osteoclast-associated protein expression, no effect on osteogenic protein expression, and no activation of related inflammatory protein expression. The empirical findings here reveal the great potential of Zn–Ag-based alloys for degradable biomaterials in internal fixation surgery/two-stage total joint revision surgery for patients with a high risk of postoperative infection and osteolysis.

1. Introduction

Approximately 20% of patients undergoing bone reconstruction surgery for various reasons are concerned regarding their susceptibility to postoperative infections and localized osteolysis [1]. Both orthopedic surgeons and patients are often fearful of these outcomes after surgery, especially patients with compromised immune systems. These include patients with systemic immune diseases (such as rheumatoid arthritis, systemic lupus erythematosus, and psoriasis), diabetes, tumors, trauma, malnutrition, advanced age, and those who have developed implant-related infections and are undergoing debridement [2–6], as well as patients who are or have been using oral glucocorticoids or immunosuppressive drugs. Owing to the dysfunctional immune environment, this group of patients can experience bacterial invasion in the early or early-mid postoperative period after bone reconstruction, which cannot be cleared by autoimmunity allowing bacteria to escape and easily incubate in the body until the opportunity arises for a final outbreak [7]. Conversely, this group of patients may face a constant

systemic inflammatory state, promoting continued osteoclast activation, osteolysis, and local low bone mass that is further aggravated post-infection, which was observed in our previous study [8].

Once implant-related infections occur in these patients, the treatment is extremely difficult, time-consuming, and costly under the double blow of infection and osteolysis, and limb deformity, amputation, and even death caused by failed infection control is much higher than that in other groups of people, which brings great physical and mental pain and economic burden to these patients [1,9–11]. Because of various underlying diseases and treatment stages of patients with low immunity status, it is difficult to standardize a clinical protocol to guide the continuous anti-infection and anti-osteolytic treatment for these patients during the perioperative and postoperative periods of bone reconstruction. Although the risk of infection has been reduced to a certain extent by continuous optimization of surgical procedures, shortening of operative time, and use of antibiotics in the perioperative period, the dual dilemma of postoperative infection and infection-related osteolysis in this population has not been fundamentally addressed [12]. Therefore, starting from implants, turning them from carriers of bacterial adhesion and proliferation into active antibacterial and active anti-osteolytic internal fixation materials for bone reconstruction, we are hoping to improve postoperative implant infection and associated osteolysis in this group of patients.

As a commonly used bone implant in clinical practice, metallic materials are rapidly evolving. Although traditional metal materials, including titanium (Ti) alloys, cobalt-chromium alloys, and stainless steels, can provide the necessary mechanical support during bone repair, they have gradually attracted attention owing to their limitations, such as non-degradable long-term retention in the body, inducing chronic inflammation or pain and requiring secondary removal surgery, and high elastic modulus, causing mismatch of elastic modulus at the implantation site leading to revision surgery [13]. In recent years, new biodegradable materials have been established and are expected to replace traditional metal materials as a new choice for the treatment of orthopedic diseases. Among them, biodegradable polymers, such as polyethylene glycol (PGA), poly (lactic acid) (PLA), and poly (L- or D, L-lactic acid) (PLLA/PDLLA) [14], have been widely used as orthopedic fixation implants for many years and have been approved by the FDA, but their low strength and acidic intermediate degradation products, resulting from massive erosion in the physiological environment, have limited their widespread use in clinical practice. As an alternative, results from research on biodegradable metallic materials, such as magnesium (Mg)-based implants, have been translated to clinical application after years of development [15]. *In vivo* degradation of Mg has played a beneficial role in promoting bone regeneration and accelerating bone disease healing, while clinical trials on the application of Mg-based metal screws in femoral head necrosis and distal radius fractures have achieved better results [16]. However, the degradation pattern of Mg-based implants is not satisfactory, and the gaseous products may lead to cavitation and inflammatory reactions, which should be further optimized [17].

In the last decade, our team has made efforts to address this goal by developing and evaluating Mg-copper (Cu) alloys that can replace conventional antibiotic bone cements for the treatment of osteomyelitis [18]. Further, we have investigated copper-containing stainless steel and Ti alloy materials with anti-bacterial adhesion [19–22]. However, the above materials either degrade too quickly to be used as internal fixation materials or do not degrade and have weak antibacterial abilities. Moreover, other teams incorporated Cu or silver (Ag) ions into orthopedic and oral implant materials such as Ti, stainless steel (SS), and Mg alloys, to impart them with bactericide properties, and obtained results similar to our study [23–35]. Biodegradable Zn alloys have been proposed as promising orthopedic implants in the last few years owing to their excellent combination of strength and ductility, appropriate degradation rates, and beneficial roles of their degradation products [33–36].

In our preliminary study, we developed and evaluated the possibility of using eight zinc (Zn)-based binary alloys as orthopedic implant materials [37], among which Zn–Cu and Zn–Ag alloys exhibited anti-infection potential. Our preliminary study suggested that the Zn–Cu alloy could be used as an anti-infective material, but it could not be used as an orthopedic internal fixation material owing to insufficient active resistance to osteolysis [37,38]. In contrast, our preliminary study showed that the Zn–Ag alloy, as an anti-infective material, can release Zn and Ag ions around the implant through degradation, and the degradation products can effectively diffuse into the tissues around the implant site, thus, promoting osseointegration. Therefore, we speculate that the Zn–Ag alloy may be an ideal antibacterial and anti-osteolytic internal fixation material for use in bone repair procedures in patients with low immunity. Other teams have conducted impressive research. They have exploited the high elongation properties of Zn4Ag–Zn8Ag alloys and Ag-containing Zn alloys to prepare scaffolds for cardiovascular use or exploited the antimicrobial properties of these alloys to explore activity against oral microorganisms or *E. coli* [39–41]. To date, no study has systematically evaluated the ability of Zn–Ag alloys to resist bone-associated infections, prevent osteolysis, and aid internal fixation of fractures.

In this study, we employed three classical animal models of anti-infection, anti-osteolysis, and internal fixation fracture repair to answer the following questions: 1. Do Zn–Ag alloys display significant anti-infection properties *in vivo* and *in vitro*? 2. Do Zn–Ag alloys display significant resistance to osteolysis of osteoclasts *in vivo* and *in vitro*? 3. Are Zn–Ag alloys as effective as Ti internal fixation screws in the treatment of femoral condylar fractures *in vivo*?

2. Materials and methods

2.1. Preparation of Zn–Ag alloy and extraction solution

The metal raw materials used in this study were prepared by mixing high-purity Zn powder (99.99%) and Ag powder (99.99%) according to different mass percentages as required. Pure Zn, Zn-0.5Ag alloy, Zn–1Ag alloy, and Zn–2Ag alloy were prepared according to the mass ratio of Ag elements of 0, 0.5%, 1%, and 2%, respectively. The metal ingots were well homogenized (350 °C, 48 h) and water quenched before extrusion. The samples were insulated at 260 °C for 2 h before extrusion, and the extrusion ratio was 36 at an extrusion rate of 1 mm/s. Bars with a final diameter of 10 mm were extruded. The metal rods were cut into disks ($\Phi 10 \times 1$ mm) and cylinders ($\Phi 1.5 \times 20$ mm), mechanically polished to 2000 mesh, subsequently cleaned via sonication in acetone and ethanol, and dried at room temperature. Prior to cellular and animal experiments, samples were sterilized using the ethylene oxide method, provided by the Sterilization and Supply Center of the Ninth People's Hospital, Shanghai Jiao Tong University School of Medicine.

The extraction solution was prepared according to the ISO10993 standard. The pure Zn and Zn–Ag alloy metal sheets were immersed in the prepared α-MEM cell culture solution at a ratio of 1.25 mL/cm^2 specific surface area and transferred to 37 °C, 5% CO_2. The extracts were collected 24 h later, filtered through sterile filter heads, placed at 4 °C, and stored for use within 3 days.

2.2. Material characterization

2.2.1. Mechanical tests

Samples for tensile tests and compressive tests were obtained along the extrusion direction according to ASTM-E8-04a and ASTM-E9-89 and carried out in a universal material test machine (Instron 5969, USA) at room temperature. For tensile and compressive tests, the displacement rates were 1×10^{-4}/s and 2×10^{-4}/s, respectively. The yield strength was determined as the stress at which the 0.2% plastic deformation occurred. The maximum stress before a 50% compressive strain was defined as ultimate compressive strength. An average of at least five

measurements was performed for each group.

2.2.2. Electrochemical tests

The electrochemical tests were conducted in an electrochemical working station (Autolab, Metrohm, Switzerland) at 37 °C in SBF solution (NaCl 8.035 g/L, NaHCO$_3$ 0.355 g/L, KCl 0.25 g/L, K$_2$HPO$_4$.3H$_2$O 0.231 g/L, MgCl$_2$.6H$_2$O 0.311 g/L, HCl 39 mL/L, CaCl$_2$ 0.292 g/L, Na$_2$SO$_4$ 0.072 g/L, Tris 6.118 g/L, pH 7.4). A three-electrode cell with a counter electrode made of platinum and a saturated calomel electrode (SCE) as the reference electrode were used. The open-circuit potential (OCP) was monitored for 5400 s for each sample. Electrochemical impedance spectroscopy (EIS) was performed by applying a 10 mV perturbation with a frequency ranging from 10^5 Hz down to 10^{-2} Hz. Potentiodynamic polarization was carried out at a scan rate of 1 mV/s, ranging from −500 mV to 500 mV (vs. OCP), and with a test area of 0.2826 cm^2. The corrosion potential (E_{corr}) and corrosion current density (i_{corr}) were calculated by linear fit and Tafel extrapolation. An average of at least five measurements was performed for each group.

2.2.3. Immersion tests

Samples were immersed in SBF solutions at 37 °C for 30 days with a volume-to-area ratio of 20 mL/cm^2 according to ASTM-G31-72. The pH value was monitored using a pH meter (Mettler Five Easy pH FE20K), and the solution was refreshed every 48 h. After immersion, samples were rinsed by distilled water and air-dried. The corrosion morphology before and after removal of corrosion products was observed by SEM. The corrosion rates of the samples were calculated based on the weight loss according to the equation, C = Δm/ρAt, where C is the corrosion rate in mm/year, Δm is the weight loss, ρ is the density of the material, A is the initial implant surface area, and t is the implantation time. An average of at least five measurements was performed for each group.

2.3. Evaluation of in vitro antibacterial activity of Zn–Ag alloys

2.3.1. Selection and culture of bacteria

To fit the orthopedic clinical infection scenario, four different strains were used in this part of the study: ATCC 25923 (*Staphylococcus aureus*), ATCC 35984 (*Staphylococcus epidermidis*), ATCC 43300 (methicillin-resistant *Staphylococcus aureus*, MRSA), and methicillin-resistant *Staphylococcus epidermidis* MRSE 287, isolated from the surface of the prosthesis of a patient with postoperative prosthesis infection at the Ninth People's Hospital of Shanghai Jiao Tong University. Monoclonal colonies were obtained after recovery of the strains, cultured in TSB medium, centrifuged, and the bacterial sediment was collected and adjusted to a concentration of 1 × 10^6 CFU/mL.

2.3.2. Evaluation of antimicrobial properties of material surfaces (coated plate method)

After sterilization with ethylene oxide, the metal disks (Zn–Ag alloys or pure Ti) were placed in the wells of a 24-well plate, and the surface antimicrobial properties of the materials were evaluated using the coated plate serial dilution method. One milliliter of bacterial suspension at a concentration of 1 × 10^6 CFU/mL was added to the 24-well plate, and the bacterial suspension was co-cultured with the material disks for 24 h. The metal disks were collected and gently rinsed with phosphate-buffered saline (PBS) three times. Disks were then placed in sterile glass test tubes (1 tube/tube) with TSB culture solution (0.5 mL) and an ultrasonic water washer (B3500S-MT, Branson Ultrasonics Co., Shanghai, China) was used to separate the bacteria adhering to the metal disks at 50 Hz for 20 min, diluted with an ultrasonically treated bacterial suspension in a gradient. Thereafter, we aspirated 500 μL of the suspension for uniform bacterial solution coating (TSA culture plate), followed by incubation at 37 °C in a constant temperature incubator for 24 h. After incubation, the number of colonies on TSA plates was counted to evaluate the antibacterial performance of the material.

2.3.3. Bacterial morphology on the material surface (scanning electron microscopy)

The material samples were co-cultured with the bacterial suspension for 24 h, and the morphology of the bacteria on the material surface was observed using field emission scanning electron microscopy (FESEM, Hitachi S-4800, CamScan). After removing the metal material samples, the samples were gently washed three times with PBS, placed in a 2% glutaraldehyde fixative, fixed overnight at 4 °C under refrigeration, rinsed at 4 °C with PBS, and fixed at 4 °C with 1% osmium PBS fixative for 2 h. Then, the specimens were washed again at 4 °C with PBS and dehydrated with different concentrations of alcohol (30%, 50%, 70%, 80%, 90%, 95%, 100%, and 100%). HITACHI HCP-2 critical point drying was followed by BAL-TEC ion sputtering and scanning electron microscopy to observe the bacterial morphology on the surface of the material.

2.3.4. Suspension inhibition performance (live dead bacteria staining)

One milliliter of bacterial suspension at a concentration of 1 × 10^6 CFU/mL was added to a 24-well plate and co-cultured with metal disks for 24 h. The bacterial suspension was collected and fluorescently stained using the Live/Dead stain kit (Invitrogen, Eugene, OR), which contains two staining solutions, EthD-1 and AM, in which EthD-1 causes red fluorescence in dead bacteria, while AM causes green fluorescence in live bacteria, thereby differentiating between live and dead bacteria to assess inhibition performance. After staining for 15 min at room temperature under low light, the bacteria were observed under a confocal laser scanning microscope (CLSM, Leica TCS, SP2, Germany) for live and dead staining to assess the inhibition performance of the suspension.

2.3.5. Morphological observation of suspension-inhibiting bacteria (SEM + TEM)

The material samples were co-cultured with bacteria for 24 h. The bacterial suspension was collected, centrifuged, and rinsed, followed by collection of the bacterial precipitate. Thereafter, we fixed and dehydrated the samples according to step 2.3.3 and then stored the samples in anhydrous ethanol, dried at the HITACHI HCP-2 critical point and then BAL-TEC ion sputtered to observe the bacterial morphology in field emission scanning electron microscopy. The bacterial precipitates were collected, washed with 1% sodium carbonate, centrifuged again, fixed in 2% glutaraldehyde, and photographed using transmission electron microscopy (TEM, Hitachi-7600 machine, Tokyo, Japan).

2.3.6. Detection of bacterial gene expression levels

To investigate the molecular mechanism of the antibacterial activity of the Zn–Ag alloy, based on the results of the antibacterial activity study of the Zn–Ag alloy mentioned above. We selected the Zn–2Ag alloy to study the antibacterial mechanism, and MRSA was selected as the target bacteria. The sterilized pure Ti and Zn–2Ag alloy metal disks were placed in 12-well plates, and three replicate samples were added to each group, with 2 mL of 1 × 10^6 CFU/mL bacterial suspension added to each well. After 24 h incubation at 37 °C, bacterial precipitates were collected, total bacterial RNA was extracted, and bacterial gene expression levels were detected using qPCR. We investigated the expression levels of biofilm-related genes, autolysis-related genes, cell wall synthesis-related genes, bacterial virulence-related genes, and resistance-related genes (Table S1).

2.4. Evaluation of osteoclastic inhibition by the Zn–Ag alloy

2.4.1. Cell acquisition and culture

In this study, we used the mouse preosteoblast cell line MC3T3-K to assess the cytocompatibility of pure Zn and Zn–Ag alloys *in vitro*. Bone marrow monocytes/macrophages (BMMs) were used to assess the effect of pure Zn and Zn–Ag alloys on osteoclast function. The cells were collected and incubated in a cell culture incubator (37 °C, 5% CO$_2$, saturated humidity). Three days later, the medium was semi-changed,

and 5 days later, the cells reached 90% confluency in the culture dish. The resulting cells were primary BMMs and were collected for further use.

2.4.2. Evaluation of in vitro cytocompatibility of Zn–Ag alloys

The proliferative activity of MC3T3-K cells was assessed using CCK-8 (Cell Counting Kit-8, Dojindo Molecular Technology, Japan). Cells were resuspended and counted, and the cell concentration was adjusted to 2×10^4 cells/mL. Equal amounts of cells were inoculated in 96-well plates (100 μL per well) and incubated in a cell culture incubator (37 °C, 5% CO_2, saturated humidity) for 2–4 h. After the cells had adhered, different dilutions of pure Zn, Zn-0.5Ag, Zn–1Ag, and Zn–2Ag alloy extracts (the extracts were supplemented with 10% FBS and 1% double antibodies) were added. The α-MEM medium (supplemented with 10% FBS, 1% double antibodies) was used as a blank control, and five replicate wells of each group were tested after 24 h and 72 h of co-culture, respectively.

2.4.3. TRAP staining to assess mature osteoclasts

BMM cells were counted and inoculated into 96-well plates (density 8×10^3 cells/well). Culture medium (100 μL of α-MEM) containing M-CSF (30 ng/mL) was added to each well and the cells were well homogenized and incubated overnight in an incubator (37 °C, 5% CO_2, saturated humidity). The next day, the upper layer of medium was aspirated and discarded, and α-MEM cell medium containing pure Zn or Zn–Ag alloy extract (containing 50 ng/mL RANKL and 30 ng/mL M-CSF) was added for induction, and the medium was changed every other day. After culturing for 5–7 days, microscopic osteoclast morphology was observed using light microscopy, while osteoclasts were identified by TRAP staining (Sigma, USA).

2.4.4. Osteoclast bone resorption study

Calf bone slices were placed in 96-well plates and inoculated with BMM cells at a concentration of 8×10^3 cells/well. Culture medium (100 μL of α-MEM) containing 30 ng/mL M-CSF was added, and cells were well homogenized and incubated overnight in a cell culture incubator (37 °C, 5% CO_2, saturated humidity). The next day, the top layer of the medium was discarded, and α-MEM culture medium (containing 50 ng/mL RANKL and 30 ng/mL M-CSF) was added. The medium was changed every other day and incubated continuously for 4 days. When the medium was changed again, α-MEM cell medium containing pure Zn and Zn–Ag alloy extract (containing 50 ng/mL RANKL and 30 ng/mL M-CSF) was added for induction. The medium was changed every other day, and incubation continued for 2 days. The bone fragments were then removed, washed, and fixed, and the bone resorption on the surface of the bone fragments was observed using SEM after gradient dehydration.

2.4.5. Osteoclast-related gene expression PCR assay

BMM cells were cultured according to the method described in section 2.4.3, collected, and total RNA was extracted using a RNeasy mini kit (Qiagen, Germany) according to the manufacturer's instructions. β-actin was used as an internal reference, and mRNA levels of osteoclast marker genes (*TRAP*, *Cts K*, *CTR*) in BMM cells were detected using qPCR. The primer sequences used are listed in Table S2. RNA (1 mg) was reverse transcribed using a reverse transcription kit (SuperScriptTM III Reverse Transcriptase), and then SYBR Premix Ex *Taq*II (2 ×) was used as the PCR reagent in an ABI 7500 Fast machine (Applied Biosystems, Courtaboeuf, France) for qPCR assays. The reaction conditions were as follows: 95 °C for 30 s; 95 °C for 5 s + 60 °C for 40 s; 40 cycles of 95 °C for 15 s, 60 °C for 1 min, and 95 °C for 15 s. The results were calculated using the $2^{-\Delta\Delta Ct}$ method.

2.5. Assessment of in vivo antibacterial ability of the Zn–Ag alloy (osteomyelitis prevention model in rat femur)

2.5.1. Surgical modeling process

Based on the results of *in vitro* studies, we chose the Zn–2Ag alloy for

in vivo antibacterial evaluation. Three-month-old male Sprague–Dawley rats were selected as the experimental animals. All experimental procedures were approved by the Animal Ethics Committee of Rat & Mouse Biotech Co. Ltd, Shanghai, China. The Zn–2Ag alloy was prepared as a $\Phi 1.5 \times 20$ mm cylinder, and a pure Ti cylinder of the same size was used as a control. After the rats were anesthetized with an intraperitoneal injection of ketamine (10 mg/kg) and 2% xylazine, the right hind limb was prepared, the knee joint was fixed in the maximum flexion position, a 15 mm longitudinal incision was made along the lateral aspect of the patella under aseptic conditions, tissues were separated layer by layer to reveal the femoral condyles, and a 1.5 mm drill was used to drill a hole in the center of the femoral condyles along the direction of the medullary cavity. Afterward, a cylindrical material (Zn–2Ag alloy or pure Ti) soaked in MRSA bacterial suspension at a concentration of 1×10^7 CFU/mL for 10 min was implanted into the femoral medullary cavity with sterile forceps, the bone wax was sealed, and the incision was closed layer by layer. Buprenorphine (0.3 mg/kg, Temgesic, Reckitt & Cloman, Hull, UK) was injected subcutaneously for postoperative analgesia. Forty rats were divided into three groups: 12 in the sham-operated group, where the wound was closed directly after incision in healthy rats and used as a blank control; 14 in the pure Ti control group, where pure Ti cylindrical material was soaked in the bacterial suspension; and 14 in the Zn–2Ag experimental group, where cylindrical Zn–2Ag alloy material was soaked in bacterial suspension. The rats in each group were euthanized at 3 and 6 weeks postoperatively.

2.5.2. X-ray observation

Radiographs of the rat femur were taken 3 and 6 weeks after surgery to evaluate the infection of the femoral medullary cavity.

2.5.3. Bacterial detection around implants

Implants and surrounding bone tissue were taken at 3 and 6 weeks postoperatively, and coated plate counting was performed after ultrasound separation of bacteria to assess the *in vivo* antimicrobial effect of Zn–2Ag.

2.5.4. Histomorphometric analysis

At 3 and 6 weeks after surgery, the rats in each group were euthanized and the right femur was removed. Rat femur specimens were fixed in 4% paraformaldehyde and decalcified in 10% EDTA for approximately 6 weeks before staining soft tissue sections. After dehydration in an ethanol gradient and embedding in paraffin, the sections were stained with hematoxylin–eosin (HE), Masson, and Gram stain to assess infection prevention. After staining was completed, the sections were observed under a high-resolution microscope (Olympus CKX41, Olympus Co. Ltd., Tokyo, Japan) and photographed.

2.5.5. General condition and hematological indicators of experimental animals

After surgery, the rats were placed back in their cages and fed a normal diet without restricting their activities. Wound healing and vital signs were regularly monitored. Blood was collected from rat hearts for routine blood tests before sampling at 6 weeks after surgery, and the systemic infection status of the rats was assessed using hematological indices.

2.6. In vivo assessment of anti-osteoclast activity of Zn–Ag alloy (Ti particle-induced cranial osteolysis model in mice)

Eight-week-old C57BL/6 mice were selected to establish a Ti particle-induced mouse cranial osteolysis model to assess the *in vivo* anti-osteoclast activity of the Zn–Ag alloy. Ti particles were washed with anhydrous ethanol for 48 h to remove endotoxins and prepared into a 300 mg/mL suspension using sterile PBS. A Ti particle suspension (0.1 mL) was injected into the subperiosteum of the mouse skull to establish an osteolysis model. PBS or Zn–2Ag extract was injected subperiosteally

once a day, and the specimens were collected and analyzed after 14 days. Twenty experimental animals were used in this study. All experimental procedures were approved by the Animal Ethics Committee of Rat & Mouse Biotech Co. Ltd, Shanghai, China.

2.6.1. Micro-CT analysis

After sampling, the mouse skull was fixed with paraformaldehyde for 3 days. Micro-CT (Skyscan 117, Aartselaar, Belgium) was performed after removing Ti particles to avoid metallic artifacts from affecting the results. The generated images were then analyzed in 3D using the micro-CT image analysis software. A square region of interest (ROI, 3×3 mm) was selected in the center of the skull for data analysis, and the skull bone mineral density (BMD) and bone tissue volume ratio (BV/TV) within the ROI were quantified.

2.6.2. Histological assessment

The specimens were decalcified using 10% EDTA decalcification solution and embedded in paraffin after decalcification. HE, TRAP, Masson, and Van Gieson staining were performed to evaluate osteolysis. After staining, the sections were observed and photographed using a high-resolution microscope.

2.7. Study of fracture repair with Zn–Ag alloy

To evaluate the effect of the Zn–Ag alloy as an implant for fracture repair, we prepared screws using the Zn–2Ag alloy and established a rabbit femoral condylar split fracture model, in which the fracture was fixed with Zn–2Ag alloy screws and Ti alloy screws (Ti–6Al–4V) as controls to evaluate the effect of Zn–2Ag alloy screws in repairing the fracture and promoting fracture healing.

2.7.1. Surgical modeling

A New Zealand rabbit femoral condylar split-fracture model was established. The surgery was performed under aseptic conditions, ketamine (10 mg/kg, Shanghai Ziyuan Pharmaceutical Co. Ltd, Shanghai, China) and 2% xylazine (5 mg/kg, Bayer AG, Germany) were injected intravenously at the ear margin for anesthesia. The right hind limb was prepared, routinely disinfected and sheeted, and the femoral condyles were exposed through the lateral parapatellar approach; then, a longitudinal fracture was made on the lateral femoral condyles with a 1 mm thick swing saw, and the fracture was fixed with a Zn–2Ag alloy screw perpendicular to the fracture line. Postoperatively, buprenorphine (0.3 mg/kg, Temgesic, Reckitt & Cloman, Hull, UK) was administered subcutaneously for pain relief. A total of 20 three-month-old New Zealand rabbits were used in this step of the experiment: 10 in the Ti alloy control group and 10 in the Zn–2Ag alloy group. All experimental procedures were approved by the Animal Ethics Committee of Jiagan Biological Technology Co. Ltd, Shanghai, China.

2.7.2. Imaging evaluation

Radiographs of the fracture site were taken on the day of surgery and 3 months after surgery to assess fracture healing. At 3 months postoperatively, the femurs of the experimental animals were kept intact, fixed in paraformaldehyde, and the femoral condyles were scanned using micro-CT. The region of interest (ROI) was selected as the 1 mm peripheral area of the screw at the fracture site, and the bone-related parameters within the ROI were quantified, including bone mineral density (BMD), bone volume (BV), bone volume fraction (BV/TV), trabecular number (Tb.N), and trabecular bone thickness (Tb.Th), and trabecular separation (Tb.Sp).

2.7.3. Histomorphometric analysis

After completion of micro-CT scanning, specimens of rabbit femoral condyles were recovered for histomorphological analysis, and hard tissue sections and soft tissue sections were obtained. The specimens were fixed in paraformaldehyde, washed in water, dehydrated in ethanol, cleaned in xylene, and embedded in methyl methacrylate. The specimens were sectioned along the coronal plane at the screw position, ground, and polished to a thickness of 100 μm and then subjected to Van Gieson staining and Paragon staining to assess fracture healing and new bone formation. At the same time, specimens of rabbit femoral condyles were taken, decalcified in 10% EDTA for approximately 6 weeks, and the screws were carefully removed, dehydrated in an ethanol gradient, embedded in paraffin, sectioned, and stained with HE, Masson, and TRAP to assess fracture healing and *in vivo* osteoclastic inhibition. Immunohistochemical techniques were applied to assess osteogenesis-related proteins (ALP, Col I, OCN, and Runx-2), osteoclast marker proteins (CTR, CTS K, OPG, TRAP), and inflammatory markers (CD11b, IL-1β, IL-6, IL-10, and TNF-α) to respectively evaluate the osteogenic, osteoclast-inhibiting, and inflammatory performance of the Zn–2Ag alloy *in vivo*.

2.8. In vivo biosafety assessment of Zn–Ag alloys

In the Zn–Ag alloy rabbit femoral condyle fracture model, the vital organs (heart, liver, spleen, lung, and kidney) of the rabbit were removed, and the organs were stained with HE to assess the presence of pathological changes. At the same time, blood was collected from the heart of rabbits to determine the Zn^{2+} and Ag^+ levels, and blood biochemical tests were performed to assess organ function.

3. Results

3.1. Material characterization

The mechanical properties and corrosion behavior of Zn–Ag alloys with pure Zn as control are presented in Fig. 1. Alloying with 1 and 2 wt % Ag significantly increased the tensile strength of Zn while maintaining its good ductility (Fig. 1a). In contrast, the compressive strength of Zn–Ag alloys decreased compared with that of pure Zn. Electrochemical tests (Fig. 1b) showed that the Zn potential shifted negatively after adding Ag, while its corrosion current density increased greatly. The electrochemical impedance spectra showed that the impedance semicircle radii of Zn–1Ag and Zn–2Ag alloys were smaller than that of pure Zn, indicating a reduced corrosion resistance. The corrosion morphology of experimental samples after immersion in SBF solution for 30 days is shown in Fig. 1c. Pure Zn was almost intact after immersion but more precipitates were found on the surface of Zn–Ag alloys. After removal of the corrosion products, pronounced corrosion was observed in Zn–Ag alloys. The intermetallic phases were relatively intact, while the surrounding Zn matrix was severely corroded, indicating a typical galvanic corrosion process. Addition of Ag accelerated the corrosion rate, with Zn-0.5Ag presenting the highest corrosion rate.

3.2. Evaluation of in vitro antibacterial activity of Zn–Ag alloys

3.2.1. Surface antibacterial performance of Zn–Ag alloy (coated plate method)

After collecting the bacteria on the surface of the material after ultrasonic shock and dilution of the coated plate, the growth status of four different bacteria, ATCC 25923, ATCC 43300, ATCC 35984, and MRSE 287, after 24 h of bacterial incubation is shown in Fig. 2a. Many bacterial monoclonal colonies were observed in the pure Ti group, suggesting that pure Ti displays no antibacterial ability. In the Zn–Ag alloy, the number of bacterial colonies in the Zn-0.5Ag alloy group was significantly less than that in the pure Zn and pure Ti groups, suggesting an obvious antibacterial performance. There was almost no bacterial colony formation in the Zn–2Ag alloy group, suggesting a good material surface antimicrobial performance of the Zn–2Ag alloy. Fig. 2b shows the quantitative results of the bacterial coated plates, and we observed that Zn–1Ag and Zn–2Ag exhibited excellent antibacterial activity. We subsequently focused on evaluating the antibacterial performance of
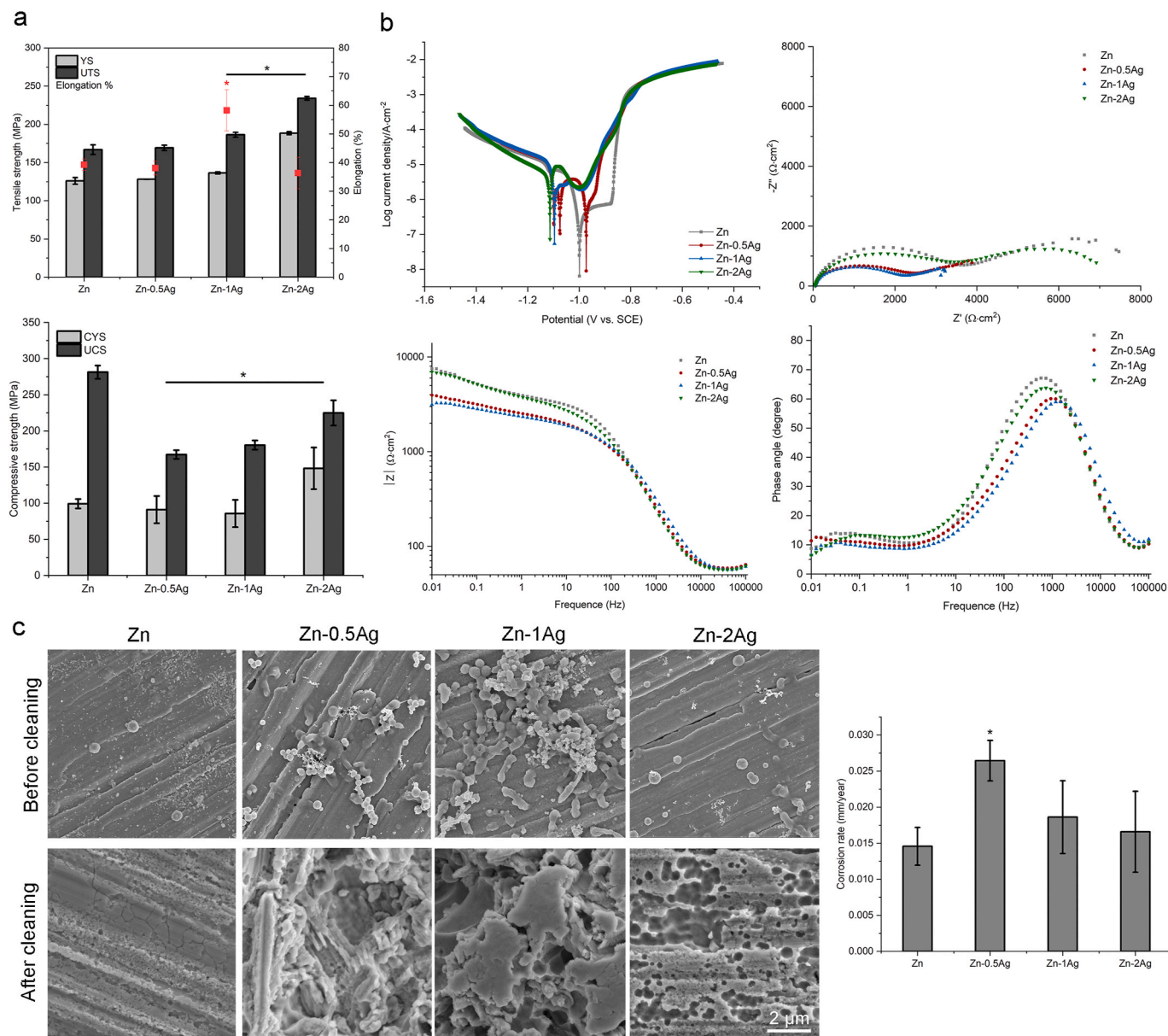
Fig. 1. Mechanical properties and corrosion behavior of Zn–Ag alloys. (a) Mechanical tests: Alloying with 1 and 2 wt% Ag significantly increased the tensile strength of Zn, while maintaining its good ductility; the compressive strength of Zn–Ag alloys decreased compared with that of pure Zn. (b) Electrochemical tests: Electrochemical tests showed that the Zn potential shifted negatively after adding Ag, while its corrosion current density increased greatly. The electrochemical impedance spectra showed that the impedance semicircle radii of Zn–1Ag and Zn–2Ag alloys were smaller than that of pure Zn, indicating a reduced corrosion resistance. (c) Immersion tests: Pure Zn was almost intact after immersion. More precipitates were found on the surface of Zn–Ag alloys. After removal of the corrosion products, pronounced corrosion was observed in Zn–Ag alloys. The intermetallic phases were relatively intact, while the surrounding Zn matrix was severely corroded, indicating a typical galvanic corrosion process. Addition of Ag accelerated the corrosion rate, with Zn-0.5Ag presenting the highest corrosion rate.

Zn–1Ag and Zn–2Ag alloys.

3.2.2. Observation of the morphology of bacteria adhering to the material surface

For this, we selected two drug-resistant bacteria, ATCC 43300 and MRSE 287, and observed the adhesion of both bacteria on the surface of each group of materials using scanning electron microscopy (Fig. 2c). The pure Ti group demonstrated that many bacteria adhered to the surface, showing colony-like growth and multi-layer bacterial stacking, suggesting the formation of bacterial biofilms. However, the number of bacteria on the surface of the pure Zn material was significantly reduced, and a small amount of degradation products were seen to encircle the bacteria. Under high magnification, bacteria appeared to break down, and the deformed bacterial morphology was observed, while only

sporadic bacterial adhesion was observed on the surface of the Zn–1Ag alloy and very little bacterial adhesion was observed on the surface of the Zn–2Ag alloy, suggesting excellent antibacterial performance of the Zn–Ag alloy.

3.2.3. Antibacterial performance of Zn–Ag alloy bacterial suspensions

The Zn–Ag alloy disks were co-cultured with the bacterial suspension for 24 h, and the bacteria in the suspension were stained to determine the ratio of live/dead bacteria. The results were observed using laser confocal microscopy (Leica TCS, SP2, Germany), as shown in Figure S1. In the live/dead bacterial staining, the live bacteria were represented by green fluorescence, while red fluorescence indicated dead bacteria. In the pure Ti group, a very strong green fluorescence was visible, suggesting many live bacterial residues, whereas in the pure Zn group, the
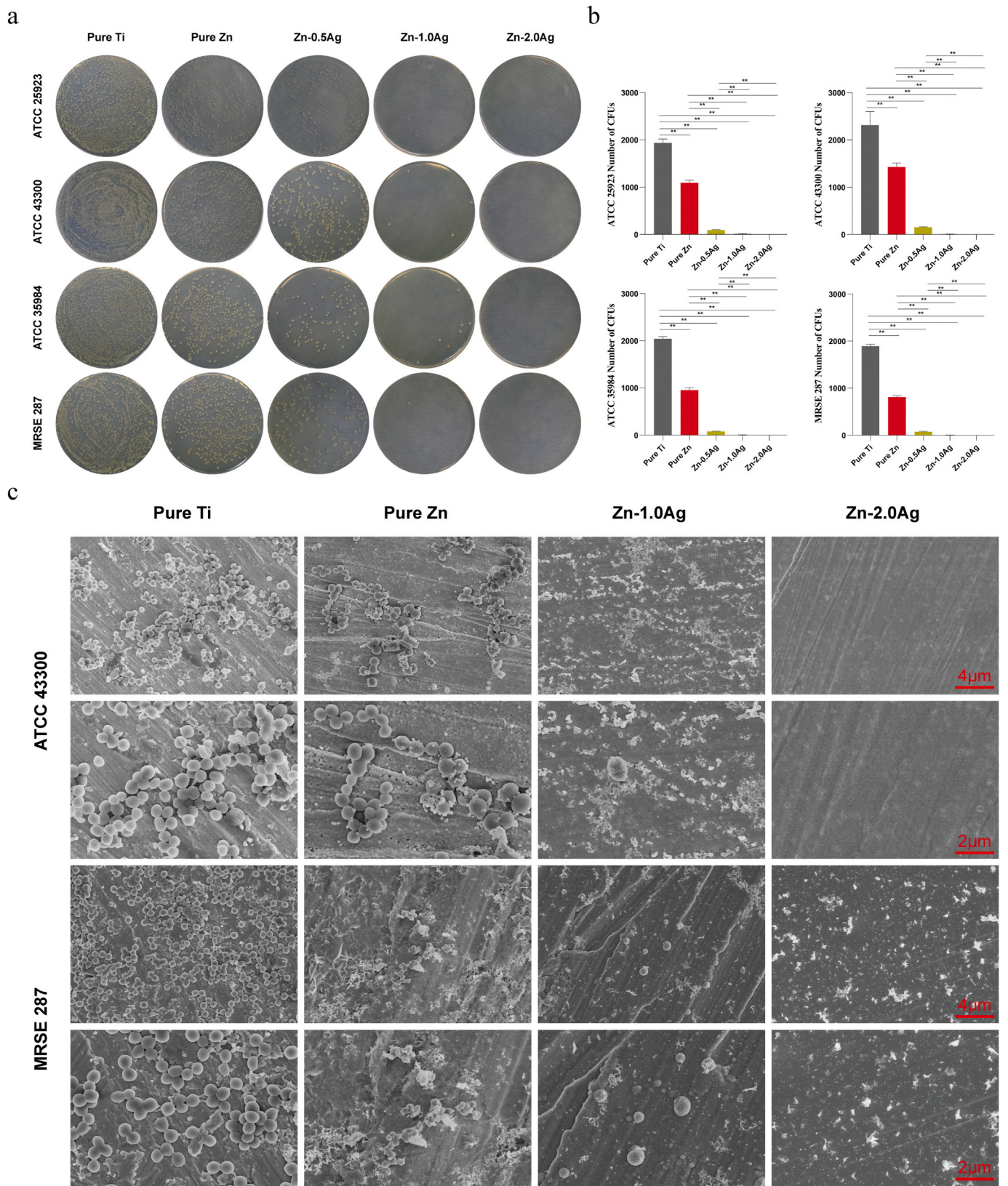
Fig. 2. *In vitro* antibacterial performances of Zn–Ag alloys. (a) Representative images of bacteria grown on the surface of samples after 24 h of culture, with pure Ti as control. (b) Colony counts of ATCC25923, ATCC43300, ATCC35984, and MRSE287 bacteria on the sample surfaces after 24 h of culture. (c) Bacterial morphologies of the ATCC43300 and MRSE287 strains on sample surfaces after 24 h of culture, with pure Ti as the control. (Data presented as mean $\pm$ SD, **p < 0.01).

green fluorescence intensity appeared slightly decreased, suggesting fewer live bacteria, indicating a slightly stronger antibacterial performance by pure Zn. In the Zn–1Ag alloy and Zn–2Ag alloy groups, a very small amount of green fluorescence was visible, suggesting fewer live bacterial residues, further verifying the good antibacterial effect of Zn–1Ag and Zn–2Ag alloys.

We also observed the morphology of bacteria in the suspension. The results of scanning electron microscopy (SEM) and transmission electron microscopy (TEM) are shown in.Figure S2 The SEM results showed that the pure Ti and pure Zn groups grew in clusters and no significant abnormalities in the bacterial morphology were observed. In contrast, in the Zn–1Ag alloy group and Zn–2Ag alloy group, bacteria were sporadically distributed and appeared "crinkled"; in the Zn–2Ag alloy group, many degradation products were observed to be wrapped around
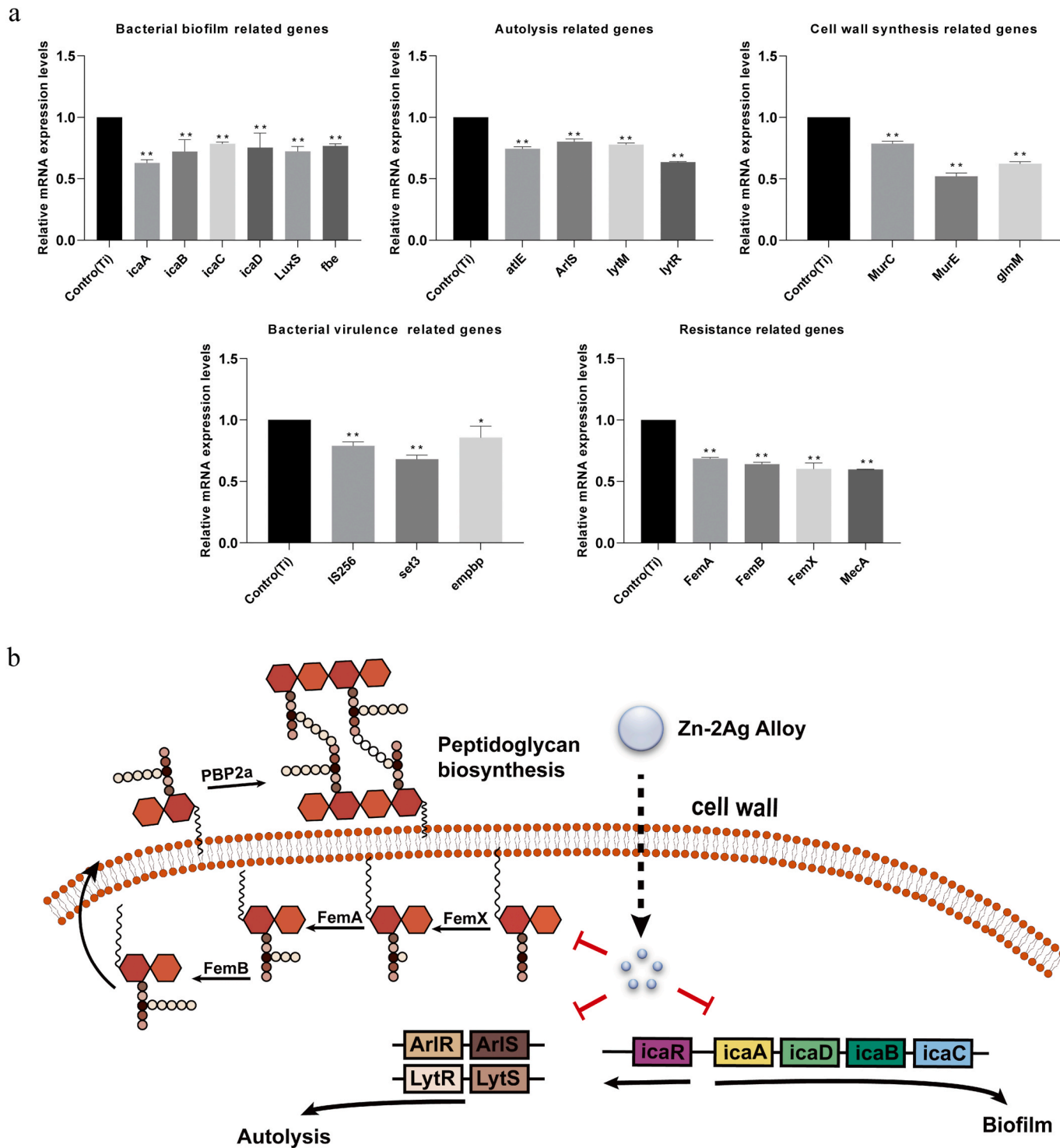
Fig. 3. Exploration of the bactericidal mechanism of Zn–2Ag alloy against MRSA. (a) Quantitative reverse-transcription polymerase chain reaction (PCR) analysis of genes associated with biofilm formation (*icaA, icaB, icaC, icaD, Luxs, fbe*), autolysis (*atlE, ArlS, lytM, lytR, atlE*), cell wall synthesis (*MurC, MurE, glmM*), bacterial virulence (*IS256, set3, empbp*), and drug-resistance (*FemA, FemB, FemX*). The mRNA levels are the relative mRNA levels compared with those in the Ti control group. (b) Possible bactericidal mechanism of Zn–2Ag alloy. (Data presented as mean $\pm$ SD; *p < 0.05, **p < 0.01).

X. Qu et al.

Bioactive Materials 6 (2021) 4607–4624

the bacteria, and the integrity of the bacteria was destroyed. TEM results further verified this conclusion. No significant changes in bacterial morphology were observed in the pure Ti and pure Zn groups, while "crinkled" bacterial morphology was observed in the Zn–1Ag and Zn–2Ag alloy groups, while edematous bands were visible in the bacterial wall envelope with abnormal bacterial morphology.

3.2.4. Effect of the Zn–Ag alloy on the expression of genes related to the behavior of MRSA bacteria

To investigate the bactericidal mechanism of the Zn–Ag alloy, we used MRSA (ATCC 43300) as the study object and selected pure Ti as the control group to observe the effect of the Zn–2Ag alloy on the expression of genes related to MRSA bacterial behavior (Fig. 3a). The results
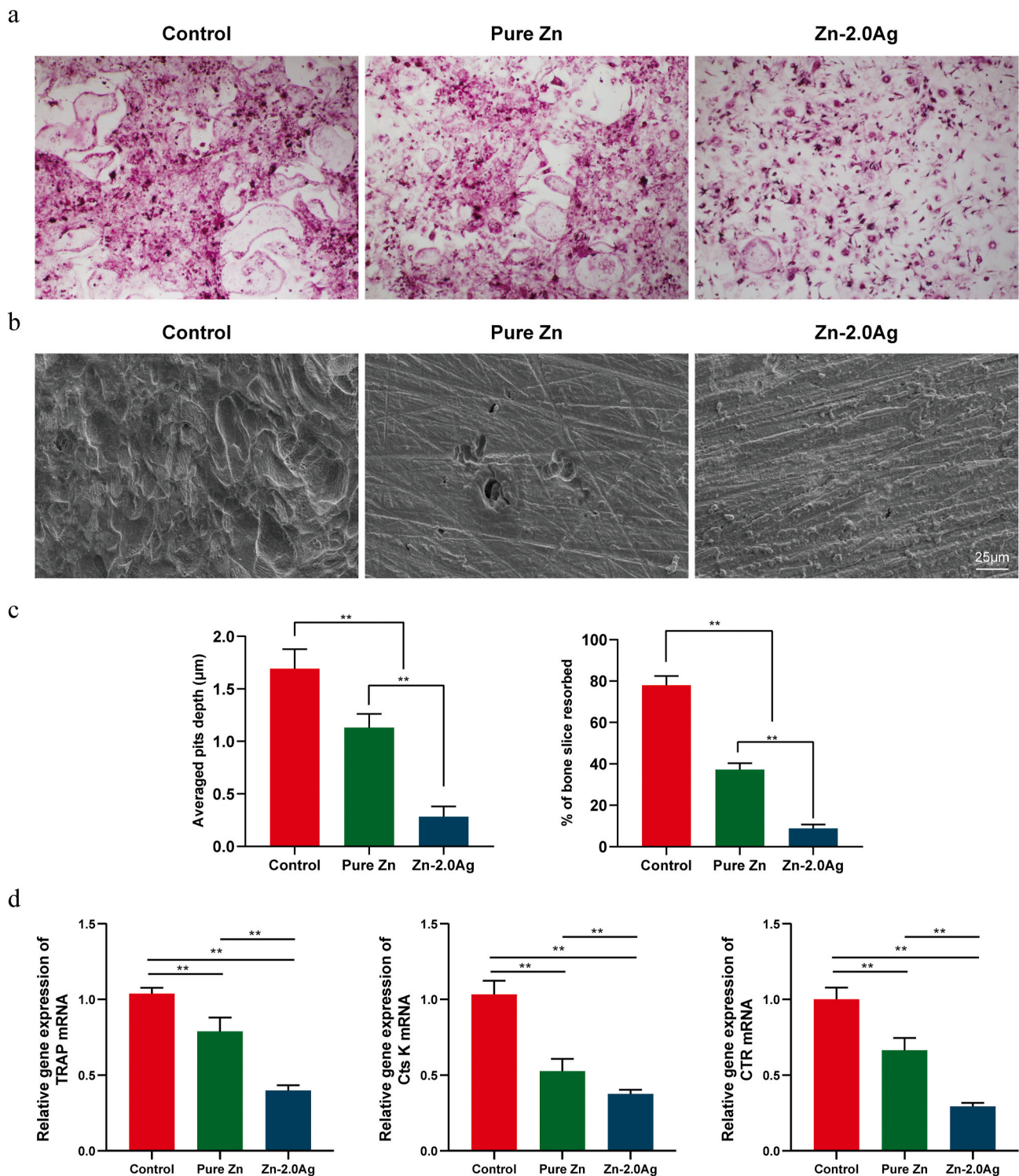

Fig. 4. Zn–2Ag alloy extract inhibits RANKL-induced osteoclast formation, bone absorption, and osteoclast-specific gene expression. (a) Bone marrow macrophages (BMMs) were treated with pure Zn or Zn–2Ag alloy extract followed by M-CSF (30 ng/mL) and RANKL (50 ng/mL) stimulation for 5 days. Cells were then fixed and subjected to tartrate-resistant acid phosphatase (TRAP) staining; (b) Scanning electron microscopy (SEM) images of bone resorption pits are shown. (c) Resorption pit areas and depth were measured using Image J and are presented graphically. (d) Osteoclast-specific gene expression (TRAP, CTR, and Cts k) was analyzed by quantitative polymerase chain reaction (PCR), and the results were normalized to β-actin expression. (Data presented as mean ± SD, **p < 0.01).

4615

showed significantly suppressed expression of biofilm-related genes (*icaA, icaB, icaC, icaD, Luxs, fbe*), autolysis-related genes (*atlE, ArlS, lytM, lytR, atlE*), cell wall synthesis-related genes (*MurC, MurE, glmM*), bacterial virulence-related genes (*IS256, set3, empbp*), and drug-resistance-related genes (*FemA, FemB, FemX*). The possible bactericidal mechanism of the Zn–2Ag alloy is shown in Fig. 3b. The Zn–2Ag alloy can play a bactericidal role by disrupting cell wall production and inhibiting bacterial autolysis biofilm formation, while effectively inhibiting bacterial virulence and improving bacterial drug resistance.

3.3. Results of in vitro cellular experiments with the Zn–Ag alloy

3.3.1. In vitro cytocompatibility performance of Zn–Ag alloys

The results of the cell proliferation activity of MC3T3-K cells co-cultured with different concentrations of Zn–Ag alloy extracts for 24 h and 72 h are shown in Figure S3. After co-culture for 24 h, only the cell proliferation activity of the 1-fold dilution group was significantly different, while no significant differences were noted in the other groups. After co-culture for 72 h, the cell proliferation activity of each
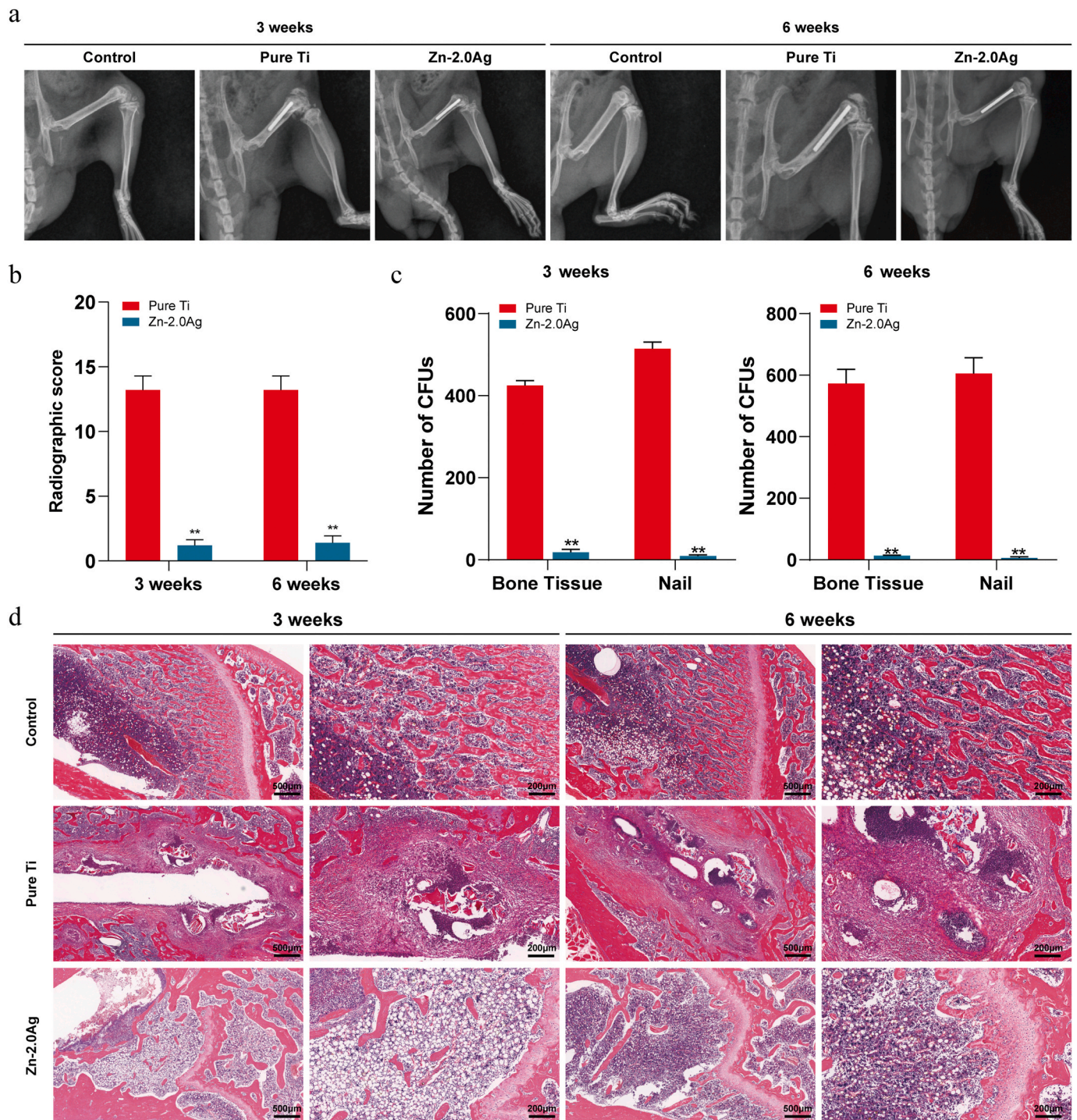

Fig. 5. Zn–2Ag alloy implants could effectively prevent MRSA-induced femoral osteomyelitis in rats. (a) Digital X-ray images and quantitative results of the rat femurs at indicated times; (b) number of bacterial colonies of bacterial cultures (peri-implant bone tissues and implanted nails) obtained using the sonication method at 3 and 6 weeks. (c) Hematoxylin–eosin (HE) staining of longitudinal sections of the rat femur at 3 and 6 weeks after implantation of Ti and Zn–2Ag intramedullary nails; MRSA-induced infection was almost completely suppressed in the Zn–2Ag group. (Data presented as mean ± SD, **p < 0.01).

Zn–Ag alloy group was significantly higher than that of the blank control group and the pure Zn control group, and a similar trend was observed under different dilutions. With increasing dilution, the cell proliferation activity of the pure Zn group became similar to that of the blank control group, confirming the threshold effect of Zn^{2+} on cell proliferation activity. All groups of Zn–Ag alloys showed excellent pro-cell proliferation properties, confirming the good cytocompatibility of Zn–Ag alloys *in vitro*, indicating that the addition of Ag could effectively optimize the poor cytocompatibility of pure Zn.

3.3.2. Zn–2Ag alloy can effectively inhibit osteoclast differentiation and bone resorption behavior

The fusion of mononuclear macrophages results in the formation of osteoclasts, and this differentiation process is influenced by the density and proliferation rate of mononuclear macrophages. Therefore, to study the effect of Zn alloy extract on osteoclast differentiation, cytotoxic effects should be excluded first. Therefore, in this section, we chose a 2-fold dilution of the Zn alloy extract. Pure Zn and Zn–2Ag alloy extracts were added during the induction of osteoclast differentiation, and the results of TRAP staining after 5 days are shown in Fig. 4a, indicating that pure Zn extracts reduced osteoclast differentiation to some extent, but the differentiation area did not differ significantly from the control group, while relative to the pure Zn group and the control group, Zn–2Ag extracts significantly reduced the TRAP-positive staining of osteoclast number and area.

Further, we investigated the effect of the Zn–2Ag alloy extract on the bone resorption function of osteoclasts (Fig. 4b). The SEM results showed that many bone resorption traps were visible in the control group, while the pure Zn group displayed significantly fewer and more superficial bone resorption traps. The Zn–2Ag alloy extract group showed even better performance than the pure Zn group (Fig. 4c), further confirming that the Zn–2Ag extract can effectively inhibit osteoclast bone resorption *in vitro*.

The expression levels of osteoclast differentiation-specific genes (*TRAP, Cts K, and CTR*) are shown in Fig. 4d. Expression levels of *TRAP, Cts K,* and *CTR* were significantly inhibited in the Zn–2Ag alloy extract group compared with the control group, which further confirms that Zn–2Ag alloy extract can inhibit osteoclast differentiation *in vitro*.

3.4. Evaluation of the in vivo resistance of Zn–Ag alloys to infection

3.4.1. Imaging assessment results

The rats in the sham-operated group showed a clear and continuous bone cortex with normal bone density (Fig. 5a and b). In contrast, the rats in the Ti group showed obvious signs of osteomyelitis, with bone cortex destruction, periosteal reaction, and double line sign, suggesting obvious chronic osteomyelitis. Rats in the Zn–2Ag alloy group showed significantly milder signs of osteomyelitis in the femur, which confirmed the good *in vivo* anti-infection ability of the Zn–2Ag alloy.

3.4.2. Bacterial culture results of implants and surrounding bone tissue

The implants and surrounding bone tissue were removed at the time of sampling, and the number of bacterial colonies of the dilution plate coating after ultrasonic shock are shown in Fig. 5c. At 3 and 6 weeks postoperatively, a large number of bacteria remained on the surface of the intramedullary nail and in the surrounding bone tissue in the Ti group, and many bacterial colonies grew after plate coating. In the Zn–2Ag group, only very few bacteria remained in the surrounding bone tissue, and no bacteria remained on the surface of the intramedullary nail, confirming the good *in vivo* antibacterial properties. Quantitative counting further confirmed this result.

3.4.3. Results of in vivo histological evaluation of Zn–Ag alloy

At 3 and 6 weeks after the modeling procedure, experimental animals were euthanized, and rat femurs were removed intact, and decalcified soft tissue sections were obtained after removal of the

intramedullary nail. In the HE staining (Fig. 5d), the femur of the rats in the Ti group showed obvious signs of infection, with many infiltrating inflammatory cells and abscess formation. In contrast, in the Zn–2Ag alloy group, the MRSA-induced infection was almost completely suppressed. Normal metaphyseal structures and normal adipocytes were visible in the medullary cavity. It was suggested that in the Zn–2Ag alloy group, MRSA infection was prevented through bactericidal effects of the alloy, and no osteomyelitis formation was observed, confirming the excellent antibacterial properties of Zn–2Ag alloy *in vivo*. The results of Masson staining and Gram staining of rat femurs at 6 weeks postoperatively are shown in Figure S4, and both Zn–2Ag alloy groups showed significantly milder signs of infection, which further confirmed the antibacterial activity of the Zn–2Ag alloy *in vivo*.

3.4.4. Hematological evaluation in rats

Hematological indices of rats in each group 6 weeks postoperatively are shown in Table S3, indicating that the WBC, NETU%, and NETU# of experimental rats in the pure Ti group were significantly higher than those in the Zn–2Ag group and the blank control group. WBC and NEUT# were significantly higher than those in the Zn–2Ag group (**$p < 0.01$). This suggests significantly heavier signs of systemic infection in the pure Ti group compared to the Zn–2Ag group, further confirming the *in vivo* antibacterial properties of the Zn–2Ag alloy.

3.5. Evaluation of in vivo anti-osteolytic activity of the Zn–Ag alloy

3.5.1. Micro-CT results

The results of micro-CT reconstruction are shown in Fig. 6a. The cranial surface of normal mice appeared flat and smooth, and no bone resorption holes or bone destruction was observed. The addition of Ti particles significantly induced cranial osteolysis in mice, with a large range of bone resorption holes visible on the cranial surface and cranial suture fracture, suggesting increased osteolysis. Cranial osteolysis was effectively inhibited by the topical application of the pure Zn extract compared with that in the Ti particle group. Osteolysis was further improved when the Zn–2Ag alloy extract was applied via local injection. The results of the quantitative analysis of micro-CT (Fig. 6b) confirmed that the Zn–2Ag alloy effectively inhibited cranial osteolysis induced by Ti particles.

3.5.2. Histomorphological results

Further histomorphometric analysis similarly confirmed the inhibition of osteoclastic osteolysis by the Zn–2Ag alloy extract. HE staining results (Fig. 6c) suggested that Ti particles led to massive bone destruction and that the dissolved bone exhibited inflammatory cell and fibrous tissue infiltration. In the Zn–2Ag alloy extract group, the inflammatory cell and fibrous tissue infiltration was significantly less than that in the Ti particle group and the pure Zn extract group, while bone destruction was slight, suggesting that the Zn–2Ag alloy extract effectively inhibited Ti particle-induced osteolysis. TRAP staining results also showed fewer positive osteoclasts in the Zn–2Ag alloy extract group than in the Ti particle and the pure Zn extract groups. In addition, active osteoclasts display high bone metabolism and a high amount of immature bone. Furthermore, Masson and Van Gieson staining (Figure S5) suggested that although mature bone was seen in the control group, a large amount of immature bone was seen in the Ti particle group, and in between the Zn–2Ag alloy extract group, which further confirmed that the Zn–2Ag alloy extract effectively inhibited the osteoclast bone resorption effect.

3.6. Zn–2Ag alloy screws for repair of femoral condylar fractures in rabbits

3.6.1. Imaging findings

The radiographic results of femoral condylar fractures in the rabbits are shown in Fig. 7a. The postoperative radiographic results showed
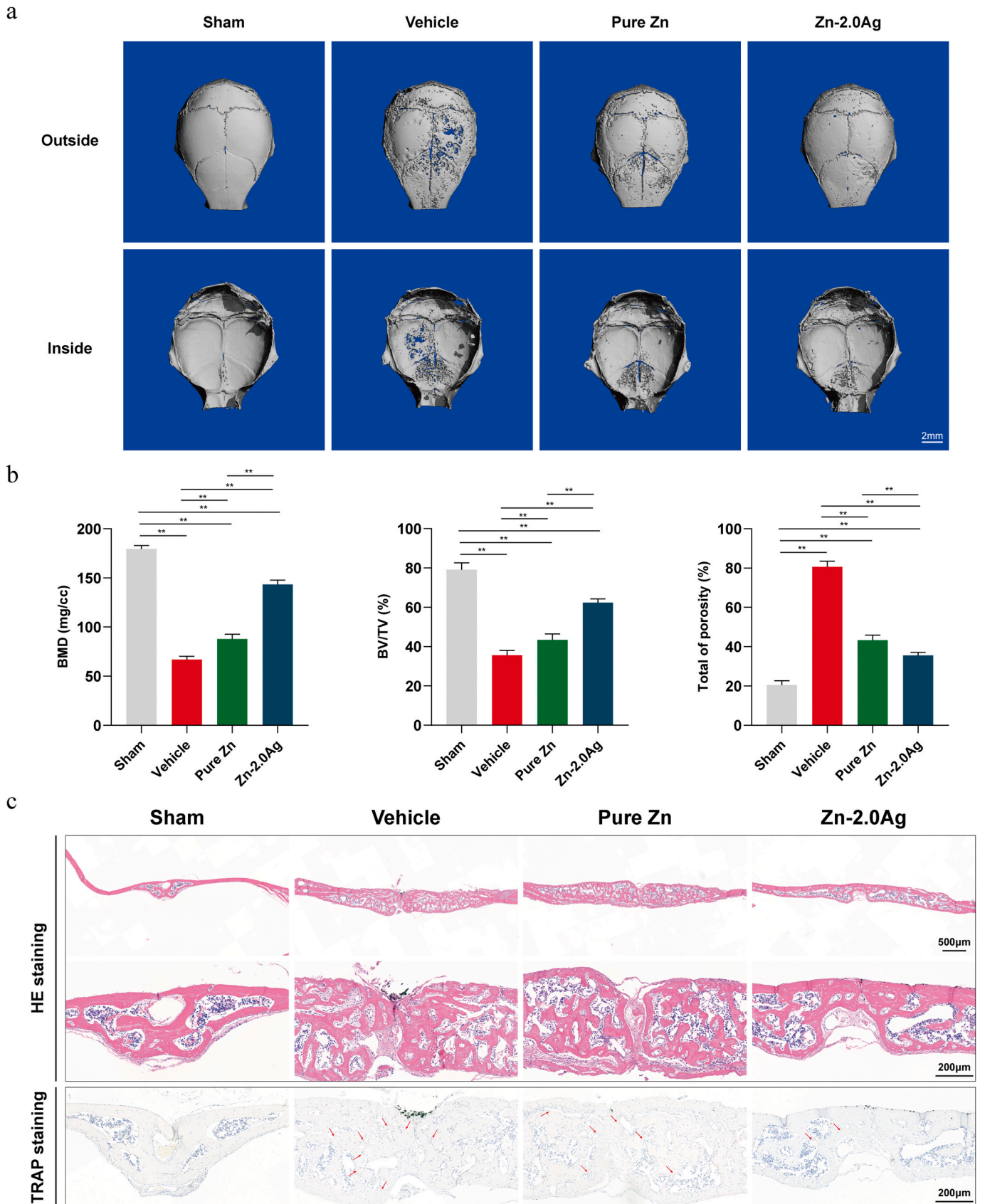
Fig. 6. Zn–2Ag alloy extract ameliorates wear Ti particle-induced osteolysis in mice calvaria. (a) Representative microtomography (micro-CT) images of the calvaria in each group. (b) Bone mineral density (BMD), bone volume to tissue volume (BV/TV), and percentage of porosity of the ROI (% total porosity). (c) Representative hematoxylin–eosin (HE)- and tartrate-resistant acid phosphatase (TRAP)-stained histological slices. (Data presented as mean $\pm$ SD, **$p < 0.01$).
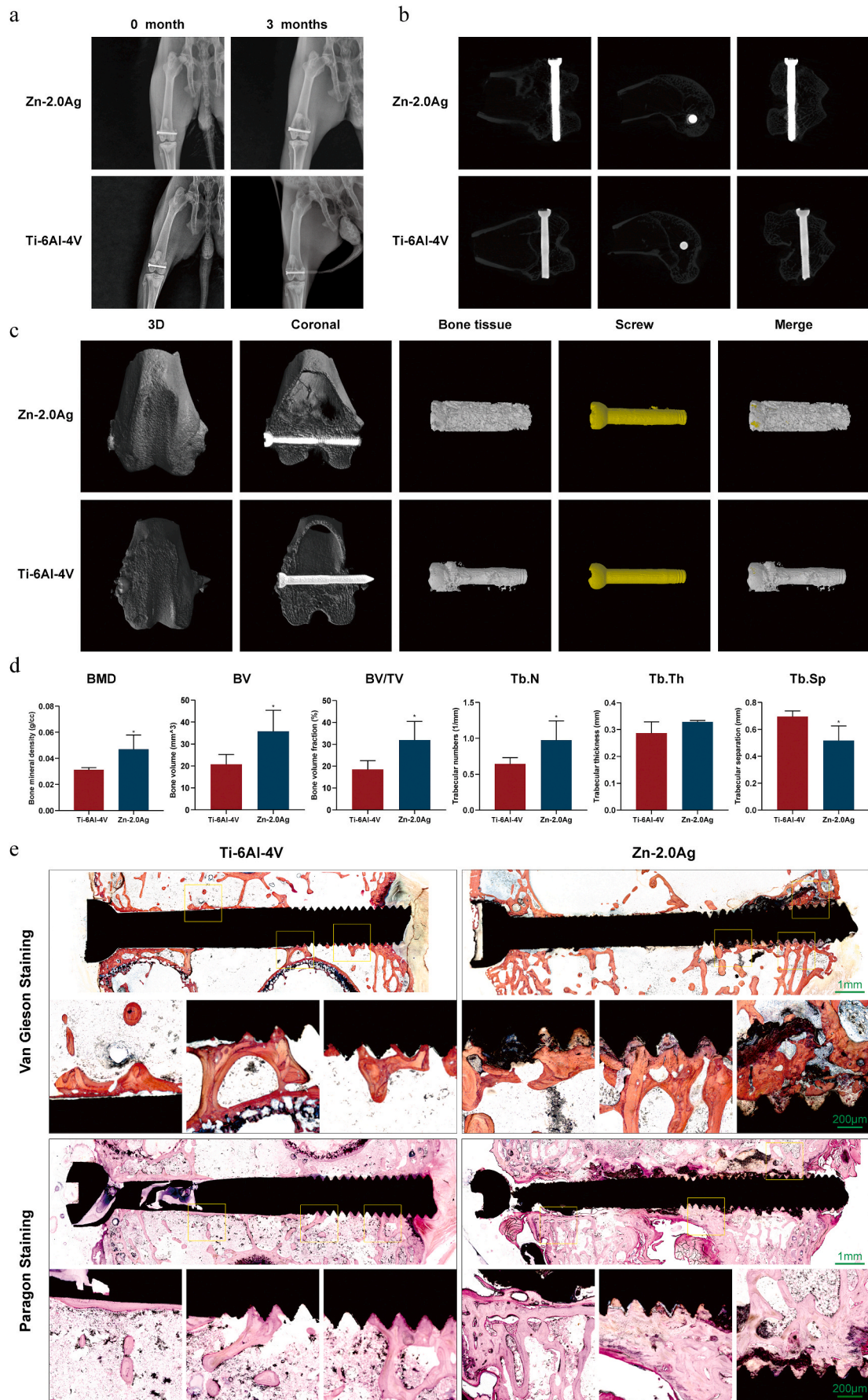
(caption on next page)

Fig. 7. Zn–2Ag alloy screws for the repair of femoral condylar split fractures in rabbits, with Ti–6Al–4V screws as control. (a) Radiographic results of the femoral condyles in rabbits immediately after the operation and 3 months after the operation, showing that the fractures had healed in both groups 3 months post-operation. (b) Micro-CT 2D scan results and (c) 3D reconstruction results of the femoral condyles of both specimens at 3 months after the operation, as well as (d) quantitative analysis of the indicators related to new bone within the ROI, which showed that both groups of fractures had healed and there was a higher amount of new bone around the Zn–2Ag alloy screws. (e) Results of Van Gieson and Paragon staining of hard tissue sections of the femoral condyles from both groups at 3 months post-operation showing that the Zn–2Ag alloy group exhibited better osseointegration and more new bone than the Ti–6Al–4V group. (Data presented as mean ± SD; *p < 0.05, **p < 0.01).

longitudinal fracture lines on the lateral side of the femoral condyle, and both Zn–2Ag alloy screws and Ti–6Al–4V alloy screws repaired the fractures well, with fracture ends well-repositioned. Three months after

surgery, both groups of condylar fractures had healed, and no obvious fracture lines were observed. Fig. 7b shows the results of micro-CT two-dimensional reconstruction 3 months post-surgery, indicating that both
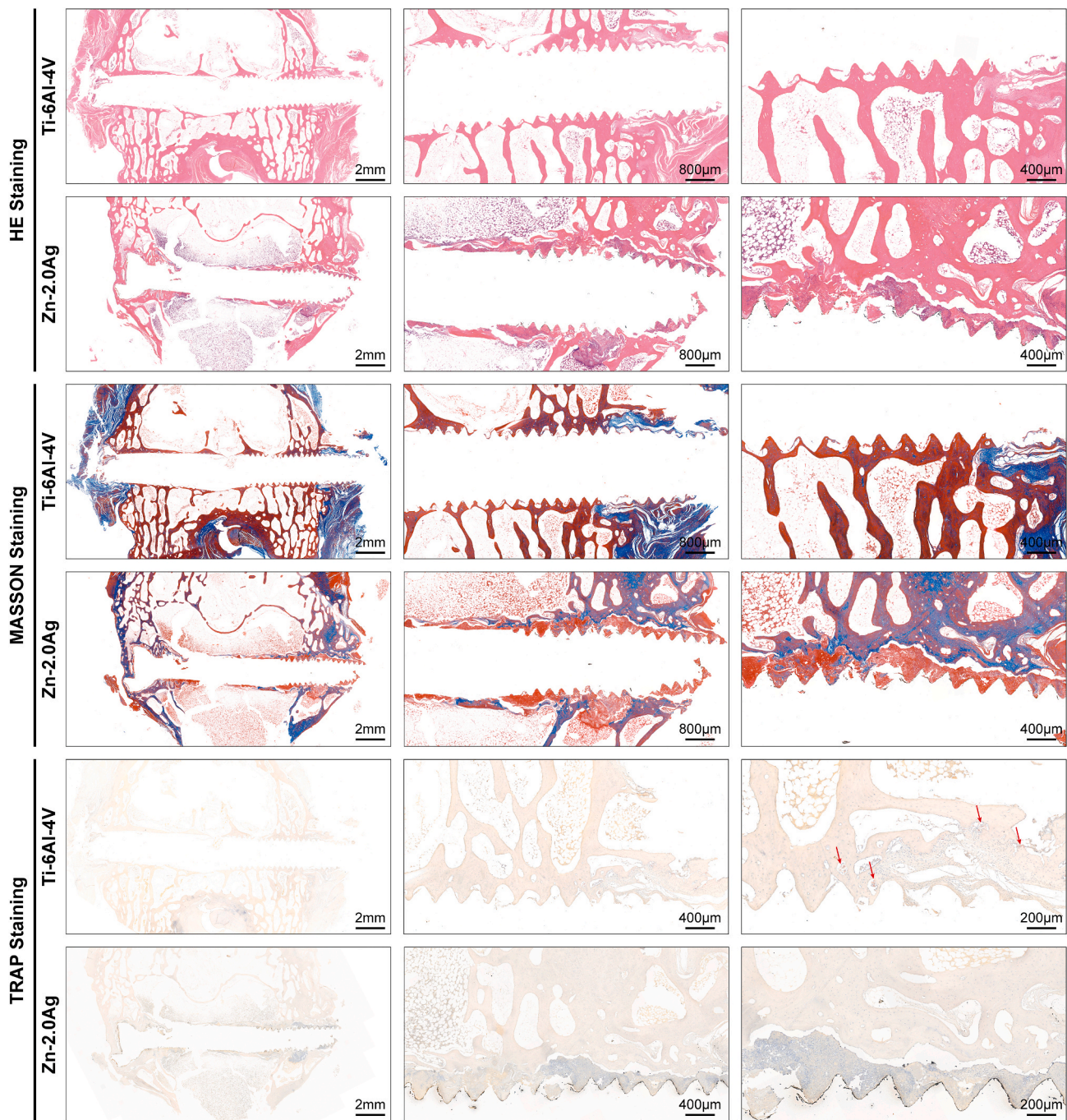

Fig. 8. Results of hematoxylin–eosin (HE), Masson, and tartrate-resistant acid phosphatase (TRAP) staining of soft tissue sections from the Zn–2Ag alloy group and the Ti–6Al–4V group at 3 months post-operation. Degradation products and new bone tissue were observed at the threads of Zn–2Ag screws with HE and Masson staining, while significantly more positive osteoclasts were seen in the Ti–6Al–4V group with TRAP staining, further indicating that Zn–2Ag alloy could effectively inhibit osteoclast activity.

groups of fractures had healed. The 3D reconstruction results of the femoral condyles showed new bone tissue around the Zn–2Ag alloy screws while the fractures were healing (Fig. 7c), suggesting that the Zn–2Ag alloy effectively promoted fracture healing while repairing fractures. Quantitative micro-CT analysis (Fig. 7d) further confirmed this result.

3.6.2. Histological assessment results

The results of hard tissue sections of the fracture repair in the Zn–2Ag alloy group and the Ti–6Al–4V alloy group 3 months postoperatively are shown in Fig. 7e. Van Gieson staining revealed many degradation products around the Zn–2Ag alloy screws and new bone around the Zn–2Ag alloy screws. We also observed good osseointegration in the threads of the Zn–2Ag alloy screws under high magnification. Paragon staining results further confirmed that the Zn–2Ag alloy screw effectively promoted osseointegration, while no significant local inflammatory reaction was observed, suggesting that the Zn–2Ag alloy screw exhibited good biocompatibility *in vivo*. Soft tissue section results are shown in Fig. 8. The HE staining and Masson staining results showed that both Zn–2Ag alloy screws and Ti–6Al–4V alloy effectively repaired the femoral condylar fractures in rabbits, and degradation products and new bone tissue were seen at the threads of the Zn–2Ag alloy. TRAP staining results revealed significantly more positive osteoclasts in the Ti–6Al–4V alloy group, while there were few positive osteoclasts in the Zn–2Ag alloy group, which further confirmed that the Zn–2Ag alloy effectively inhibited osteoclast activity. The immunohistochemical results of osteogenesis-related indexes are shown in Figure S6a. However, expression of osteoclast-related indexes in the Zn–2Ag alloy group was lower than that in the Ti–6Al–4V alloy group (Figure S6b), indicating that the Zn–2Ag alloy effectively inhibited osteoclast activity *in vivo*. Furthermore, expression levels of inflammation-related indicators are shown in Figure S7, and no enhanced expression of each inflammation indicator was observed in the Zn–2Ag alloy group compared with the Ti–6Al–4V alloy group, suggesting that the Zn–2Ag alloy does not induce inflammatory reactions *in vivo*, which indicates good biocompatibility of the Zn–2Ag alloy *in vivo*.

3.7. Results of in vivo biosafety assessment of Zn–Ag alloys

The staining results of rabbit organ sections 3 months postoperatively are shown in Figure S8: no pathological changes were observed in sections of the pure Ti control group or in the Zn–2Ag alloy group. The results of rabbit blood biochemistry and ion concentration 3 months after surgery are shown in Figure S9: no significant difference was observed between the two groups of animals, indicating no abnormalities in vital organ function in the experimental animals.

4. Discussion

This study addresses the characteristics of high-risk orthopedic patients who are prone to postoperative infection and bone loss. Based on our previous studies [37,38], a biodegradable orthopedic internal fixation material with both antibacterial and osteolysis inhibiting properties, Zn–Ag alloy, was developed. Unlike most recent studies on biodegradable metals for orthopedic implants, this study established three classical animal models for antibacterial, anti-osteolysis, and fracture internal fixation and illustrated the effects and possible mechanisms of Zn–Ag from multiple perspectives. The potential of the Zn–Ag alloy as an internal fixation material for fractures was demonstrated.

In the case of the Zn–2Ag alloy, our preliminary study showed that Ag exists in both the solid solution and AgZn$_3$ phase in Zn–2Ag alloy. Moreover, the solid solution matrix corroded preferentially, followed by the AgZn$_3$ phase. Therefore, it is reasonable to expect the release of Ag ions from both the matrix and AgZn$_3$ phases during the *in vivo* degradation. Additionally, the major degradation product of Zn–2Ag alloy *in vivo* is ZnO. Meanwhile, we failed to identify any solid degradation

products containing Ag, indicating the release of Ag ions into the surrounding tissue. Furthermore, Zn–Ag alloys presented good mechanical strength while maintaining an excellent elongation rate. It was reported that Ag can activate the pyramidal $<c+a>$ slip systems to maintain a high fracture elongation [42]. Considering this, Zn–Ag alloy can be used as an anti-infective material by releasing Zn and Ag ions around the implant during degradation, and the degradation products can effectively diffuse into the tissues around the implant site without affecting, or even promoting, osseointegration and inhibiting osteolysis.

We prepared the Zn–Ag alloy and found that the addition of Ag could greatly improve the antibacterial ability of Zn-based materials: 1) the bactericidal effect was significant against the most common pathogenic bacteria of orthopedic clinical infections, even drug-resistant bacteria, such as MRSA and MRSE (Fig. 2); and 2) the occurrence of osteomyelitis was inhibited in the *in vivo* antibacterial experiments, and the advantages in imaging and bacteriological and histological tests were obvious (Fig. 5). However, there is a lack of sufficient information regarding the potential antibacterial mechanism of the Zn–Ag alloy. Inhibition of biofilm formation is important for the prevention and treatment of infections. Biofilm formation is divided into two steps: bacterial colonization of the material surface and secretion of the extracellular matrix by colonized bacteria to encapsulate the bacterium [43,44]. Genes affecting bacterial adhesion colonization include *Alte* [45], which encodes a cell wall autolysin that mediates direct adhesion through hydrophobic changes, and *Fbe* [46], which encodes a fibrinogen-binding protein that is highly homologous to the bacterial wall surface protein ClfB and mediates bacterial adhesion. In addition, the thickening phase of the biofilm is mainly mediated by the polysaccharide intercellular adhesion element (PIA) and by mechanisms independent of PIA. The main genes encoding PIA are *icaA, icaD, icaB,* and *icaC*, which are negatively regulated by *icaR* [43]. In addition, QS was found to be closely related to the biofilm construction process and biofilm antibiotic resistance [47], while Luxs regulate the synthesis of the quorum sensing signal molecule AI-2, and bacterial biofilm formation is diminished by gene deletion. Bacterial autolysis similarly affects biofilm formation [48], as evidenced by bacterial lysis and extracellular DNA release, which is important in regulating early adhesion of bacteria to implant surfaces and other bacteria and plays an important role in stabilizing biofilm structure in mature bacterial biofilms. The main reason for the formation of MRSA bacterial biofilms is the creation of a suitable living environment for partner bacteria through the autolytic sacrifice of some MRSA bacteria, which provides the basis for biofilm formation. By downregulating *Alte, Fbe, icaA, icaD, icaB,* and *icaC* and inhibiting autolysis-related gene expression, the Zn–Ag alloy significantly inhibited several steps of biofilm formation. However, bacterial virulence genes encode related bacterial toxin synthesis, which is directly responsible for local tissue destruction and systemic inflammatory toxic response at the onset of infection, and the Zn–Ag alloy significantly downregulated related gene expression levels (*IS256, set3, empbp*). The prevalence of drug-resistant bacteria has become a clinical challenge in recent years, with MRSA being the most common bone-associated infectious disease. Staphylococcal resistance to methicillin is mainly attributed to the presence of *mecA* [49], which encodes novel penicillin-binding protein 2a (PBP2a), a low-affinity penicillin-binding protein, while related studies have shown that femA, femB, and FemX are associated with *mecA* and are involved in the expression of methicillin resistance. The Zn–Ag alloy significantly downregulates expression of resistance genes and that of *mecA*, *femA*, *femB*, *FemX*, and others, which is expected to relieve the "crisis" of drug-resistant bacteria in clinical practice and is expected to further improve the efficacy of bone infection in combination with antibiotics.

In our previous study, we established a rabbit osteomyelitis model and proved that bacterial infection is an important cause of bone loss, especially in infections with high concentrations of staphylococci [8]. Infectious bone destruction seriously affects bone biomechanics and function and even leads to pathological fracture, which is a serious

sequela of infection. Infection-associated bone loss is characterized by the presence of abnormally activated osteoclasts. The Zn–Ag alloy significantly inhibited osteoclastic differentiation of BMM cells *in vitro*, as evidenced by attenuated TRAP staining and significant down-regulation of osteoclast-related genes (*TRAP, CTSK, CTR*), while in a mouse cranial osteolysis model, micro-CT data yielded a significant increase in bone volume and bone density after treatment with the Zn–Ag alloy extract compared with that in the control group. A significant decrease in positively activated osteoclasts was observed in histological TRAP staining, confirming that the Zn–2Ag alloy can effectively inhibit Ti particle-induced cranial osteolysis in mice. Both *in vitro* and *in vivo* data demonstrated the exact effect of the Zn–Ag alloy in directly inhibiting osteoclast activation. It is noteworthy that the degradation products of the ZnAg alloy under the influence of tissue and body fluids are quite different from those *in vitro*. Furthermore, we constructed a rabbit femoral condylar fracture model and observed the effect of ZnAg alloy screws on peripheral osteolysis of osteoclasts by section TRAP staining and immunohistochemical staining.

In response to the high incidence of postoperative orthopedic infections in immunocompromised patients, the development of orthopedic implants with antibacterial and reversal of infection-associated bone destruction abilities is necessary, and these functions have been well-demonstrated by Zn–Ag alloys in this study. On this basis, the osseointegration ability of the implant is crucial for further bone healing in non-infected patients and in patients with controlled bone infection [50]. We constructed a rabbit femoral condyle fracture model in *in vivo* experiments to further evaluate the osseointegration properties of the Zn–Ag alloy. Overall, the Zn–Ag alloy showed osseointegration comparable to that of the Ti–6Al–4V alloy, as evidenced by comparable new bone encapsulation around the screw in micro-CT reconstructed images and hard tissue sections (Fig. 7). The process of local bone reconstruction is not only closely related to osteoblasts but also plays an important role in osteoclastic activity, which induces the formation of mature osteoblasts and bone matrix deposition, bone remodeling, and restoration of normal physiological function of bone tissue depending on physiological osteoclastic differentiation, together determining the outcome of osseointegration [51]. First, in terms of inducing osteogenic differentiation, we utilized immunohistochemical staining of tissue sections to assess important indicators of this, namely, ALP, COL I, OCN, and Runx-2, of which ALP and Runx2 are both early osteogenic markers, while OCN and COL1 are major components of non-collagenous and collagenous proteins of bone tissue, respectively. Although darkly stained areas were seen around the screws in the Zn–Ag alloy group compared with the control group, it can be concluded that this area is a Zn-based metal degradation product and no obvious new bone tissue was observed. This darkly stained area may be due to the adsorption of staining substances by metal degradation products. In contrast, focusing on the surrounding bone tissue outside the degradation products, no significantly increased expression of the above-mentioned osteogenic differentiation indexes was observed, and it was concluded that the Zn–Ag alloy did not have the ability to directly stimulate osteogenic differentiation. In addition, osteoclastic differentiation of bone tissue determines osseointegration outcome. Although the excellent ability of the Zn–Ag alloy to inhibit osteoclastic activation has been demonstrated in mouse cranial osteolysis experiments, this study further evaluated the performance of the Zn–Ag alloy in fracture healing models by observing the expression of important osteoclast-related genes (*CTR, CTSK, OPG, TRAP*) through TRAP staining and immunohistochemistry. More TRAP-stained positive osteoclast cells were distributed around the Ti–6Al–4V alloy, while immunohistochemical analysis showed darkly stained areas in the tissues around the screws, suggesting abnormal activation of osteoclastic differentiation. In contrast, in the Zn–Ag alloy group, TRAP-stained positive osteoclasts were rare, except for the deep staining in the degradation product area, and no obvious areas of high expression were seen in the immunohistochemical results. Combined with the aforementioned analysis regarding disadvantages of

conventional inert metal materials, the long-term presence of non-degradable metals may cause an inflammatory response around the implant, ultimately leading to abnormally activated osteoclastic differentiation. In contrast, in a study of degradable implants, it was found that the acidic environment caused by the degradation of organic polymorphic materials, such as PGA, PLA, and PLLA/PDLLA [52], the gas released and the alkaline microenvironment caused by the degradation of Mg-based degradable metals can lead to abnormally activated inflammatory responses [53,54]. Although the Zn–Ag alloy in this study also showed obvious degradation behaviors *in vivo*, no significant inflammatory activation was observed by immunohistochemical staining of inflammation-related indicators (CD11b, IL-1β, IL-6, IL-10, TNF-α), again demonstrating excellent degradation safety and suggesting that the lack of inflammatory response activation by the Zn–Ag alloy during degradation is an important reason for the inhibition of osteoclastic differentiation and good osseointegration performance. Therefore, although the Zn–Ag alloy did not show significant activation of osteogenic differentiation in the fracture healing model, its good biodegradability and the lack of inflammatory response caused by the degradation products were notable advantages in inhibiting osteoclastic activation and markedly promoting peri-implant osseointegration.

Research on degradable metals is important to further improve the treatment of orthopedic diseases, and Zn-based alloys are currently at the forefront of research in this field because of their excellent mechanical properties and good degradability [55]. Zn-based metals have the potential to be used as a functional material in specific diseases, in addition to their traditional internal fixation or support properties [34, 37]. For example, high-strength Zn–Li alloy has been developed for fracture sites with high load-bearing capacity [56,57], Zn–Sr alloy with bi-directional regulation of osteogenesis-breakage has been developed for osteoporotic bone defects or fractures [33], and Zn–Mn and Zn–Mg alloys have been used to develop bone tissue engineering scaffolds and cardiovascular scaffolds owing to their good elongation properties [58–60]. The Zn–Ag alloy developed in this study shows significant superiority over other existing Zn-based alloys in the treatment of bone-related diseases because of its ability to resist infection, inhibit osteoclastic differentiation, and promote osseointegration, especially in postoperative orthopedic patients in low-immunity groups with a high prevalence of infection. Furthermore, this alloy has a wide range of applications.

In future clinical applications, biodegradable Zn alloys may be used for specially shaped bone defect repair or specially shaped implants. Even when the cutting preparation process for standard implants such as screws is not mature, 3D printing is the best option for cost saving. Several international teams are currently engaged in 3D printing of Zn-based metals and have done excellent work [61–63].

5. Conclusion

For patients with internal fixation surgery/two-stage total joint revision surgery with a high risk of postoperative infection and osteolysis, there is no targeted effective treatment, and the rate of reoperation due to infection and osteolysis remains high. In this study, we prepared Zn–Ag alloys with active antibacterial and anti-osteolytic properties. For antibacterial properties, our results indicated that the Zn–2Ag alloy inhibits coagulase-positive and -negative staphylococci, as well as antibiotic-resistant strains (MRSA and MRSE), by preventing bacterial adhesion and biofilm formation. The Zn–2Ag alloy broadly affected the expression of MRSA genes associated with autolysis, biofilm formation, and drug resistance. A rat femur osteomyelitis prevention model was established, and the Zn–2Ag alloy-treated group showed significant antibacterial activity against MRSA. For anti-osteolysis properties, the Zn–2Ag alloy significantly inhibited osteoclastic differentiation of BMM cells *in vitro*, as evidenced by attenuated TRAP staining and significant downregulation of osteoclast-related genes (TRAP, CTSK, CTR), whereas in the mouse cranial osteolysis model, micro-CT data yielded a

significant increase in bone volume and bone density after treatment with Zn–Ag alloy extracts compared with that in the control group. A significant decrease in positively activated osteoclasts was observed in histological TRAP staining sections, confirming that the Zn–2Ag alloy effectively inhibits Ti particle-induced cranial osteolysis in mice. For bone fracture fixation properties, the Zn–2Ag based screws showed similar performance in bone fracture fixation compared to the Ti–6Al–4V counterpart. The fracture healed completely after 3 months in the rabbit femoral condyle fracture model. Furthermore, TRAP staining and immunohistochemical staining for osteoclast-associated proteins showed that osteoclasts around the Zn–Ag alloy screws were significantly inhibited. The biodegradable Zn–Ag alloy offers a promising option to fill the gap in biodegradable implants in internal fixation surgery/two-stage total joint revision surgery with a high risk of postoperative infection and osteolysis applications.

Data and materials availability

All data associated with this study are present in the paper or the Supplementary Materials.

Declaration of competing interest

The authors declare no conflict of interest.

CRediT authorship contribution statement

Xinhua Qu: Conceptualization, Methodology, Investigation, Writing – original draft, Data curation. **Hongtao Yang:** Conceptualization, Methodology, Investigation, Writing – review & editing, Data curation. **Bo Jia:** Methodology, Investigation, Writing – original draft, Data curation. **Minqi Wang:** Investigation, Writing – original draft. **Bing Yue:** Writing – review & editing. **Yufeng Zheng:** Conceptualization, Methodology, Resources, Supervision, Writing – review & editing, Project administration, Funding acquisition. **Kerong Dai:** Conceptualization, Methodology, Resources, Supervision, Project administration, Funding acquisition.

Appendix B. Supplementary data

Supplementary data to this article can be found online at https://doi.org/10.1016/j.bioactmat.2021.05.023.

References

[1] D.P. Lew, F.A. Waldvogel, Osteomyelitis, Lancet (London, England) vol. 364, 2004, pp. 369–379, https://doi.org/10.1016/S0140-6736(04)16727-5, 9431.

[2] C.R. Arciola, D. Campoccia, L. Montanaro, Implant infections: adhesion, biofilm formation and immune evasion, Nature reviews, Microbiology 16 (7) (2018) 397–409, https://doi.org/10.1038/s41579-018-0019-y.

[3] P. Doshi, H. Gopalan, S. Sprague, C. Pradhan, S. Kulkarni, M. Bhandari, Incidence of infection following internal fixation of open and closed tibia fractures in India (INFINITI): a multi-centre observational cohort study, BMC Muscoskel. Disord. 18 (1) (2017) 156, https://doi.org/10.1186/s12891-017-1506-4.

[4] H. Wang, H. Pei, M. Chen, H. Wang, Incidence and predictors of surgical site infection after ORIF in calcaneus fractures, a retrospective cohort study, J. Orthop. Surg. Res. 13 (1) (2018) 293, https://doi.org/10.1186/s13018-018-1003-y.

[5] N.T. Spina, I.S. Aleem, A. Nassr, B.D. Lawrence, Surgical site infections in spine surgery: preoperative prevention strategies to minimize risk, Global Spine J. 8 (4 Suppl) (2018) 31S–36S, https://doi.org/10.1177/2192568217752130.

[6] M. Wouthuyzen-Bakker, M. Sebillotte, J. Lomas, B. Kendrick, E.B. Palomares, O. Murillo, J. Parvizi, N. Shohat, J.C. Reinoso, R.E. Sanchez, M. Fernandez-Sampedro, E. Senneville, K. Huotari, J.M.B. Allende, A.B. Garcia, J. Lora-Tamayo, M.C. Ferrari, D. Vaznaisiene, E. Yusuf, C. Aboltins, R. Trebse, M.J. Salles, N. Benito, A. Vila, M.D.D. Toro, T.S. Kramer, S. Petersdorf, V. Diaz-Brito, Z.K. Tufan, M. Sanchez, C. Arvieux, A. Soriano, E.S.G.f.I.-A. Infections, Timing of implant-removal in late acute periprosthetic joint infection: a multicenter observational study, J. Infect. 79 (3) (2019) 199–205, https://doi.org/10.1016/j.jinf.2019.07.003.

[7] J.C. Mandell, B. Khurana, J.T. Smith, G.J. Czuczman, V. Ghazikhanian, S.E. Smith, Osteomyelitis of the lower extremity: pathophysiology, imaging, and classification, with an emphasis on diabetic foot infection, Emerg. Radiol. 25 (2) (2018) 175–188, https://doi.org/10.1007/s10140-017-1564-9.

[8] H. Li, S. Zhang, S. Huo, H. Tang, B. Nie, X. Qu, B. Yue, Effects of staphylococcal infection and aseptic inflammation on bone mass and biomechanical properties in a rabbit model, J Orthop Translat 21 (2020) 66–72, https://doi.org/10.1016/j.jot.2019.11.006.

[9] M. Depypere, M. Morgenstern, R. Kuehl, E. Senneville, T.F. Moriarty, W. T. Obremskey, W. Zimmerli, A. Trampuz, K. Lagrou, W.J. Metsemakers, Pathogenesis and management of fracture-related infection, Clin. Microbiol. Infect. 26 (5) (2020) 572–578, https://doi.org/10.1016/j.cmi.2019.08.006.

[10] J.M. Schierholz, J. Beuth, Implant infections: a haven for opportunistic bacteria, J. Hosp. Infect. 49 (2) (2001) 87–93, https://doi.org/10.1053/jhin.2001.1052.

[11] W. Costerton, R. Veeh, M. Shirtliff, M. Pasmore, C. Post, G. Ehrlich, The application of biofilm science to the study and control of chronic bacterial infections, J. Clin. Invest. 112 (10) (2003) 1466–1477.

[12] Y. Wang, W. Teng, Z. Zhang, X. Zhou, Y. Ye, P. Lin, A. Liu, Y. Wu, B. Li, C. Zhang, X. Yang, W. Li, X. Yu, Z. Gou, Z. Ye, A trilogy antimicrobial strategy for multiple infections of orthopedic implants throughout their life cycle, Bioact Mater 6 (7) (2021) 1853–1866, https://doi.org/10.1016/j.bioactmat.2020.11.030.

[13] M. Prakasam, J. Locs, K. Salma-Ancane, D. Loca, A. Largeteau, L. Berzina-Cimdina, Biodegradable materials and metallic implants-A review, J. Funct. Biomater. 8 (4) (2017), https://doi.org/10.3390/jfb8040044.

[14] C. Gao, S. Peng, P. Feng, C. Shuai, Bone biomaterials and interactions with stem cells, Bone Res 5 (2017), 17059, https://doi.org/10.1038/boneres.2017.59.

[15] H. Klauser, Internal fixation of three-dimensional distal metatarsal I osteotomies in the treatment of hallux valgus deformities using biodegradable magnesium screws in comparison to titanium screws, Foot Ankle Surg. 25 (3) (2019) 398–405, https://doi.org/10.1016/j.fas.2018.02.005.

[16] D. Zhao, S. Huang, F. Lu, B. Wang, L. Yang, L. Qin, K. Yang, Y. Li, W. Li, W. Wang, S. Tian, X. Zhang, W. Gao, Z. Wang, Y. Zhang, X. Xie, J. Wang, J. Li, Vascularized bone grafting fixed by biodegradable magnesium screw for treating osteonecrosis of the femoral head, Biomaterials 81 (2016) 84–92, https://doi.org/10.1016/j.biomaterials.2015.11.038.

[17] Y.F. Zheng, X.N. Gu, F. Witte, Biodegradable metals, Mater. Sci. Eng. R Rep. 77 (2014) 1–34, https://doi.org/10.1016/j.mser.2014.01.001.

[18] Y. Li, L. Liu, P. Wan, Z. Zhai, Z. Mao, Z. Ouyang, D. Yu, Q. Sun, L. Tan, L. Ren, Z. Zhu, Y. Hao, X. Qu, K. Yang, K. Dai, Biodegradable Mg-Cu alloy implants with antibacterial activity for the treatment of osteomyelitis: in vitro and in vivo evaluations, Biomaterials 106 (2016) 250–263, https://doi.org/10.1016/j.biomaterials.2016.08.031.

[19] Y. Zhuang, L. Ren, S. Zhang, X. Wei, K. Yang, K. Dai, Antibacterial effect of a copper-containing titanium alloy against implant-associated infection induced by methicillin-resistant Staphylococcus aureus, Acta Biomater. 119 (2021) 472–484, https://doi.org/10.1016/j.actbio.2020.10.026.

[20] Y. Zhuang, S. Zhang, K. Yang, L. Ren, K. Dai, Antibacterial activity of copper-bearing 316L stainless steel for the prevention of implant-related infection, J. Biomed. Mater. Res. B Appl. Biomater. 108 (2) (2020) 484–495, https://doi.org/10.1002/jbm.b.34405.

[21] L. Wang, G. Li, L. Ren, X. Kong, Y. Wang, X. Han, W. Jiang, K. Dai, K. Yang, Y. Hao, Nano-copper-bearing stainless steel promotes fracture healing by accelerating the callus evolution process, Int. J. Nanomed. 12 (2017) 8443–8457, https://doi.org/10.2147/IJN.S146866.

[22] L. Wang, L. Ren, T. Tang, K. Dai, K. Yang, Y. Hao, A novel nano-copper-bearing stainless steel with reduced Cu(2+) release only inducing transient foreign body reaction via affecting the activity of NF-kappaB and Caspase 3, Int. J. Nanomed. 10 (2015) 6725–6739, https://doi.org/10.2147/IJN.S90249.

[23] X. Zhao, P. Wan, H. Wang, S. Zhang, J. Liu, C. Chang, K. Yang, Y. Pan, An antibacterial strategy of Mg-Cu bone grafting in infection-mediated periodontics, BioMed Res. Int. 2020 (2020), 7289208, https://doi.org/10.1155/2020/7289208.

[24] Q. Zhao, Q. Yi, A. Hu, L. Jiang, L. Hong, J. Dong, Antibacterial and osteogenic activity of a multifunctional microporous coating codoped with Mg, Cu and F on titanium, J. Mater. Chem. B 7 (14) (2019) 2284–2299, https://doi.org/10.1039/c8tb03377c.

[25] K. Yu, Y. Dai, Z. Luo, H. Long, M. Zeng, Z. Li, J. Zhu, L. Cheng, Y. Zhang, H. Liu, Y. Zhu, In vitro and in vivo evaluation of novel biodegradable Mg-Ag-Y alloys for use as resorbable bone fixation implant, J. Biomed. Mater. Res. 106 (7) (2018) 2059–2069, https://doi.org/10.1002/jbm.a.36397.

[26] D. Tie, F. Feyerabend, W.D. Muller, R. Schade, K. Liefeith, K.U. Kainer, R. Willumeit, Antibacterial biodegradable Mg-Ag alloys, Eur. Cell. Mater. 25 (2013) 284–298, https://doi.org/10.22203/ecm.v025a20, discussion 298.

[27] H. Qin, Y. Zhao, Z. An, M. Cheng, Q. Wang, T. Cheng, Q. Wang, J. Wang, Y. Jiang, X. Zhang, G. Yuan, Enhanced antibacterial properties, biocompatibility, and

corrosion resistance of degradable Mg-Nd-Zn-Zr alloy, Biomaterials 53 (2015) 211–220, https://doi.org/10.1016/j.biomaterials.2015.02.096.

[28] J. Liu, X. Zhang, H. Wang, F. Li, M. Li, K. Yang, E. Zhang, The antibacterial properties and biocompatibility of a Ti-Cu sintered alloy for biomedical application, Biomed. Mater. 9 (2) (2014), 025013, https://doi.org/10.1088/1748-6041/9/2/025013.

[29] E. Zhang, C. Liu, Effect of surface treatments on the surface morphology, corrosion property, and antibacterial property of Ti-10Cu sintered alloy, Biomed. Mater. 10 (4) (2015), 045009, https://doi.org/10.1088/1748-6041/10/4/045009.

[30] E. Zhang, J. Ren, S. Li, L. Yang, G. Qin, Optimization of mechanical properties, biocorrosion properties and antibacterial properties of as-cast Ti-Cu alloys, Biomed. Mater. 11 (6) (2016), 065001, https://doi.org/10.1088/1748-6041/11/6/065001.

[31] Z. Lei, H. Zhang, E. Zhang, J. You, X. Ma, X. Bai, Antibacterial activities and cell responses of Ti-Ag alloys with a hybrid micro- to nanostructured surface, J. Biomater. Appl. 34 (10) (2020) 1368–1380, https://doi.org/10.1177/0885328220905103.

[32] B. Bai, E. Zhang, H. Dong, J. Liu, Biocompatibility of antibacterial Ti-Cu sintered alloy: in vivo bone response, J. Mater. Sci. Mater. Med. 26 (12) (2015) 265, https://doi.org/10.1007/s10856-015-5600-6.

[33] B. Jia, H. Yang, Z. Zhang, X. Qu, X. Jia, Q. Wu, Y. Han, Y. Zheng, K. Dai, Biodegradable Zn-Sr alloy for bone regeneration in rat femoral condyle defect model: in vitro and in vivo studies, Bioact Mater 6 (6) (2021) 1588–1604, https://doi.org/10.1016/j.bioactmat.2020.11.007.

[34] Z.Z. Shi, X.X. Gao, H.J. Zhang, X.F. Liu, H.Y. Li, C. Zhou, Y.X. Yin, L.N. Wang, Design biodegradable Zn alloys: second phases and their significant influences on alloy properties, Bioact Mater 5 (2) (2020) 210–218, https://doi.org/10.1016/j.bioactmat.2020.02.010.

[35] S. Liu, D. Kent, N. Doan, M. Dargusch, G. Wang, Effects of deformation twinning on the mechanical properties of biodegradable Zn-Mg alloys, Bioact Mater 4 (1) (2019) 8–16, https://doi.org/10.1016/j.bioactmat.2018.11.001.

[36] E. Zhang, X. Zhao, J. Hu, R. Wang, S. Fu, G. Qin, Antibacterial metals and alloys for potential biomedical implants, Bioact Mater 6 (8) (2021) 2569–2612, https://doi.org/10.1016/j.bioactmat.2021.01.030.

[37] H. Yang, B. Jia, Z. Zhang, X. Qu, G. Li, W. Lin, D. Zhu, K. Dai, Y. Zheng, Alloying design of biodegradable zinc as promising bone implants for load-bearing applications, Nat. Commun. 11 (1) (2020) 401, https://doi.org/10.1038/s41467-019-14153-7.

[38] X. Qu, H. Yang, B. Jia, Z. Yu, Y. Zheng, K. Dai, Biodegradable Zn-Cu alloys show antibacterial activity against MRSA bone infection by inhibiting pathogen adhesion and biofilm formation, Acta Biomater. 117 (2020) 400–417, https://doi.org/10.1016/j.actbio.2020.09.041.

[39] P. Li, C. Schille, E. Schweizer, F. Rupp, A. Heiss, C. Legner, U.E. Klotz, J. Geis-Gerstorfer, L. Scheideler, Mechanical characteristics, in vitro degradation, cytotoxicity, and antibacterial evaluation of Zn-4.0Ag alloy as a biodegradable material, Int. J. Mol. Sci. 19 (3) (2018), https://doi.org/10.3390/ijms19030755.

[40] Z.Z. Shi, J. Yu, X.F. Liu, H.J. Zhang, D.W. Zhang, Y.X. Yin, L.N. Wang, Effects of Ag, Cu or Ca addition on microstructure and comprehensive properties of biodegradable Zn-0.8Mn alloy, Mater Sci Eng C Mater Biol Appl 99 (2019) 969–978, https://doi.org/10.1016/j.msec.2019.02.044.

[41] M. Wątroba, W. Bednarczyk, J. Kawałko, K. Mech, M. Marciszko, G. Boelter, M. Banzhaf, P. Bała, Design of novel Zn-Ag-Zr alloy with enhanced strength as a potential biodegradable implant material, Mater. Des. 183 (2019), 108154.

[42] M. Sikora-Jasinska, E. Mostaed, A. Mostaed, R. Beanland, D. Mantovani, M. Vedani, Fabrication, mechanical properties and in vitro degradation behavior of newly developed ZnAg alloys for degradable implant applications, Mater Sci Eng C Mater Biol Appl 77 (2017) 1170–1181, https://doi.org/10.1016/j.msec.2017.04.023.

[43] N.K. Archer, M.J. Mazaitis, J.W. Costerton, J.G. Leid, M.E. Powers, M.E. Shirtliff, Staphylococcus aureus biofilms, Virulence 2 (5) (2011) 445–459, https://doi.org/10.4161/viru.2.5.17724.

[44] O. Charyeva, J. Neilands, G. Svensäter, A. Wennerberg, Bacterial biofilm formation on resorbing magnesium implants, Open J. Med. Microbiol. 5 (2015) 1–11, https://doi.org/10.4236/ojmm.2015.51001, 01.

[45] S. Zhang, H. Tang, Y. Wang, B. Nie, H. Yang, W. Yuan, X. Qu, B. Yue, Antibacterial and antibiofilm effects of flufenamic acid against methicillin-resistant

Staphylococcus aureus, Pharmacol. Res. 160 (2020), 105067, https://doi.org/10.1016/j.phrs.2020.105067.

[46] A.C. Pickering, P. Vitry, V. Prystopiuk, B. Garcia, M. Höök, J. Schoenebeck, J. A. Geoghegan, Y.F. Dufrène, J.R. Fitzgerald, Host-specialized fibrinogen-binding by a bacterial surface protein promotes biofilm formation and innate immune evasion, PLoS Pathog. 15 (6) (2019), e1007816, https://doi.org/10.1371/journal.ppat.1007816.

[47] K. Papenfort, B.L. Bassler, Quorum sensing signal-response systems in Gram-negative bacteria, Nat. Rev. Microbiol. 14 (9) (2016) 576–588, https://doi.org/10.1038/nrmicro.2016.89.

[48] C. Mayer, R.M. Kluj, M. Mühleck, A. Walter, S. Unsleber, I. Hottmann, M. Borisova, Bacteria's different ways to recycle their own cell wall, Int J Med Microbiol 309 (7) (2019), 151326, https://doi.org/10.1016/j.ijmm.2019.06.006.

[49] S.J. Peacock, G.K. Paterson, Mechanisms of methicillin resistance in Staphylococcus aureus, Annu. Rev. Biochem. 84 (2015) 577–601, https://doi.org/10.1146/annurev-biochem-060614-034516.

[50] R. Agarwal, A.J. Garcia, Biomaterial strategies for engineering implants for enhanced osseointegration and bone repair, Adv. Drug Deliv. Rev. 94 (2015) 53–62, https://doi.org/10.1016/j.addr.2015.03.013.

[51] F. Shang, Y. Yu, S. Liu, L. Ming, Y. Zhang, Z. Zhou, J. Zhao, Y. Jin, Advancing application of mesenchymal stem cell-based bone tissue regeneration, Bioact Mater 6 (3) (2021) 666–683, https://doi.org/10.1016/j.bioactmat.2020.08.014.

[52] D. Zhao, T. Zhu, J. Li, L. Cui, Z. Zhang, X. Zhuang, J. Ding, Poly(lactic-co-glycolic acid)-based composite bone-substitute materials, Bioact Mater 6 (2) (2021) 346–360, https://doi.org/10.1016/j.bioactmat.2020.08.016.

[53] C. Liu, Z. Ren, Y. Xu, S. Pang, X. Zhao, Y. Zhao, Biodegradable magnesium alloys developed as bone repair materials: a review, Scanning 2018 (2018), 9216314, https://doi.org/10.1155/2018/9216314.

[54] M. Nabiyouni, T. Bruckner, H. Zhou, U. Gbureck, S.B. Bhaduri, Magnesium-based bioceramics in orthopedic applications, Acta Biomater. 66 (2018) 23–43, https://doi.org/10.1016/j.actbio.2017.11.033.

[55] H. Kabir, K. Munir, C. Wen, Y. Li, Recent research and progress of biodegradable zinc alloys and composites for biomedical applications: biomechanical and biocorrosion perspectives, Bioact Mater 6 (3) (2021) 836–879, https://doi.org/10.1016/j.bioactmat.2020.09.013.

[56] G.-N. Li, S.-M. Zhu, J.-F. Nie, Y. Zheng, Z. Sun, Investigating the stress corrosion cracking of a biodegradable Zn-0.8 wt% Li alloy in simulated body fluid, Bioactive materials 6 (5) (2021) 1468–1478.

[57] H. Yang, X. Qu, M. Wang, H. Cheng, B. Jia, J. Nie, K. Dai, Y. Zheng, Zn-0.4 Li alloy shows great potential for the fixation and healing of bone fractures at load-bearing sites, Chem. Eng. J. 417 (2021), 129317.

[58] S. Lin, X. Ran, X. Yan, Q. Wang, J.G. Zhou, T. Hu, G. Wang, Systematical evolution on a Zn-Mg alloy potentially developed for biodegradable cardiovascular stents, J. Mater. Sci. Mater. Med. 30 (11) (2019) 122, https://doi.org/10.1007/s10856-019-6324-9.

[59] W. Pachla, S. Przybysz, A. Jarzebska, M. Bieda, K. Sztwiertnia, M. Kulczyk, J. Skiba, Structural and mechanical aspects of hypoeutectic Zn-Mg binary alloys for biodegradable vascular stent applications, Bioact Mater 6 (1) (2021) 26–44, https://doi.org/10.1016/j.bioactmat.2020.07.004.

[60] B. Jia, H. Yang, Y. Han, Z. Zhang, X. Qu, Y. Zhuang, Q. Wu, Y. Zheng, K. Dai, In vitro and in vivo studies of Zn-Mn biodegradable metals designed for orthopedic applications, Acta Biomater. 108 (2020) 358–372, https://doi.org/10.1016/j.actbio.2020.03.009.

[61] Y. Li, P. Pavanram, J. Zhou, K. Lietaert, F.S.L. Bobbert, Y. Kubo, M.A. Leeflang, H. Jahr, A.A. Zadpoor, Additively manufactured functionally graded biodegradable porous zinc, Biomater Sci 8 (9) (2020) 2404–2419, https://doi.org/10.1039/c9bm01904a.

[62] Y. Li, W. Li, F.S.L. Bobbert, K. Lietaert, J.H. Dong, M.A. Leeflang, J. Zhou, A. A. Zadpoor, Corrosion fatigue behavior of additively manufactured biodegradable porous zinc, Acta Biomater. 106 (2020) 439–449, https://doi.org/10.1016/j.actbio.2020.02.001.

[63] Y. Li, P. Pavanram, J. Zhou, K. Lietaert, P. Taheri, W. Li, H. San, M.A. Leeflang, J. M.C. Mol, H. Jahr, A.A. Zadpoor, Additively manufactured biodegradable porous zinc, Acta Biomater. 101 (2020) 609–623, https://doi.org/10.1016/j.actbio.2019.10.034.